

Modeling fracture in elasto-plastic solids by embedded-discontinuity stress-hybrid finite element formulation

Jaka Dujc and Boštjan Brank

Faculty of Civil and Geodetic Engineering, University of Ljubljana, Ljubljana, Slovenia

ABSTRACT

The Hellinger-Reissner principle is applied to derive a hybrid-mixed quadrilateral finite element with embedded-discontinuity in displacements, which can model a discrete crack (interface) within the element, and its sliding (and opening). The chosen material models are elasto-plasticity with hardening for the bulk, and traction-separation plasticity with softening for the interface. The latter model describes localized material failure and relates cohesion degradation with the fracture energy. The fulfillment of the inelastic relations at the bulk's integration points is performed by a stress-driven update algorithm. The stress and embedded-discontinuity kinematic parameters are condensed on the element level, allowing for an efficient implementation.

ARTICLE HISTORY

Received 16 April 2020
Accepted 20 June 2020

KEYWORDS

2D solid; elasto-plasticity; embedded-discontinuity; fracture modeling; softening-plasticity; stress-hybrid quadrilateral

1. Introduction

Structural limit states often go along with one or more zones with cracks or slip lines where the ultimate material resistance had been reached. It has been extensively documented that this kind of localized material failures cannot be computationally modeled with the standard finite element method. To this end, various techniques have been proposed for computational modeling of nonlinear material fracture. Presently, there is a number of competitive methods, but discussing and comparing them is beyond the scope of this paper; we refer to e.g. [1] for a review. In this work, we apply the embedded-discontinuity (ED) concept initiated in 1990s, see e.g. [2] and [3], and later studied in a number of works, see e.g. [4–7] for some representative expositions. Embedded-discontinuity finite element method (ED-FEM) has been applied (with various levels of success and robustness [8, 9]) for modeling localized material failures (in static and dynamic frameworks) in 2d and 3d solids, and also in structural elements such as beams, plates and shells, mainly for brittle materials with assumed elastic bulk. We refer to e.g. [10–21] for some representative works. Among the other methods, let us mention recently introduced phase field for fracture, see e.g. [22–26]. It is a smeared crack method, which naturally deals with crack nucleation, branching and coalesce. This is in contrast with ED, which is a discrete crack method and usually needs a crack-tracking algorithm for a single track. Contrary to the smeared crack methods, the discrete crack methods represent the crack as a kinematic strong discontinuity, either between the elements (through cohesive interface) or within the elements (introducing a cohesive interface by a suitable kinematic enrichment). The phase field for fracture is easier to implement than the ED concept, but its main problem is that the resulting set of equations is

not well conditioned. It also shares other shortcomings of the smeared crack techniques, one of them being high computational costs, because very fine meshes are needed for quality results. On the other hand, ED-FEM can use rather coarse meshes, however, ED elements may exhibit locking, and the loss of robustness and reliability [21].

In this work, we use the ED concept in order to model material fracture in 2d elasto-plastic solids. In particular, we apply the Hellinger-Reissner mixed variational principle as a framework for deriving a stress-hybrid, ED quadrilateral finite element. The stress-hybrid formulation is chosen because of an accurate computation of stresses. Among different possibilities for enhancing accuracy of stress and/or strain computation for the quadrilateral, the stress-hybrid approach (with Pian-Sumihara stress approximations [27]) has been recognized as the optimal one. It is optimal in a sense that it provides excellent results already for coarse meshes and has the best stress convergence among enhanced quadrilaterals, see e.g. [28–30]. In the ED formulations, the “timing” of the slip line embedding and its direction depend on element's stress state. It is therefore important that the latter is computed as accurate as possible. On the other hand, the choice of the stress-hybrid formulation requires an application of a stress-driven algorithm for an inelastic bulk material model. The formulation that is presented in what follows combines: (a) the stress-hybrid quadrilateral with Pian-Sumihara stress approximations [27], (b) an embedded-strong-discontinuity concept for 2d solids that allows for a linear variation of the displacement-jumps along the discontinuity, (c) an elasto-plastic material model formulation for the bulk of the element that includes a stress-driven update for inelastic constitutive relations at the integration points, and (d) plasticity with

softening in the interface between two parts of the element, describing degradation of the cohesion because of slip line sliding (and opening).

The main novelty of the presented work is a stress-hybrid, ED quadrilateral for 2d solids, with hardening elasto-plasticity for the bulk and plasticity with softening for localized slip line. The formulation is an extension of the stress-hybrid, ED quadrilateral with elastic bulk proposed in [31]. The second novelty is a stress-driven update algorithm (at bulk's integration points) derived for the fulfillment of elasto-plastic constitutive relations with isotropic hardening (which is similar to the one presented in [32]). The stress parameters and the enriched kinematic parameters (describing kinematics of the slip line) are condensed on the element level. From the outside, the element's unknowns are only nodal displacements, allowing its smooth implementation into a standard finite element computer code for nonlinear structural analysis. The Petrov-Galerkin interpolation is applied, yielding a non-symmetric element's tangent stiffness matrix. As shown in [6], this kind of interpolation is necessary to avoid a spurious transition of the stresses across the embedded discontinuity at the zero-traction state.

The rest of the paper is organized as follows. In Section 2, the derivation of the finite element is explained, and in Section 3, the implementation issues of the formulation are addressed. Illustrative numerical examples are given in Section 4, and the paper is completed by conclusions in Section 5.

2. Stress-hybrid ED formulation

2.1. Kinematics

Consider a quadrilateral occupying $\Omega^e \subset \mathbb{R}^2$, as shown in Figure 1. Its geometry is defined by the bi-linear mapping $\xi \mapsto \mathbf{x}$ where $\xi \in [-1, 1] \times [-1, 1]$, $\mathbf{x} \in \Omega^e$, and

$$\mathbf{x}(\xi) = [x, y]^T = \sum_{a=1}^4 N_a(\xi) \mathbf{x}_a, \quad \mathbf{x}_a = [x_a, y_a]^T, \quad \xi = [\xi, \eta]^T, \quad (1)$$

where \mathbf{x}_a are coordinates of the node a , and N_a are Lagrange interpolations over the bi-unit square. The parameters that define element's displacements are nodal displacements $\mathbf{d}_a^e = [u_{xa}, u_{ya}]^T$, and amplitudes of the displacement-jumps α_m , $m = 1, \dots, 4$ over the line Γ^e representing internal interface (also called discontinuity in what follows). The displacement-jumps are connected with the four separation modes from Figure 2, and the line Γ^e divides element into two non overlapping sub-domains Ω^{e+} and Ω^{e-} , where $\Omega^e \setminus \Gamma^e$ is called element's bulk. The displacements are approximated over the element as:

$$\mathbf{u}(\xi, \Gamma^e)|_{\Omega^e} = [u_x, u_y]^T = \sum_{a=1}^4 N_a(\xi) \mathbf{d}_a^e + \sum_{m=1}^4 \mathbf{p}_m(\xi, \Gamma^e) \alpha_m, \quad (2)$$

where the interpolation functions for the displacement-jumps are, see [33]

$$\mathbf{p}_1 = \left(H_\Gamma(\mathbf{x}) - \sum_{a \in \Omega^{e+}} N_a \right) \mathbf{n}, \quad (3)$$

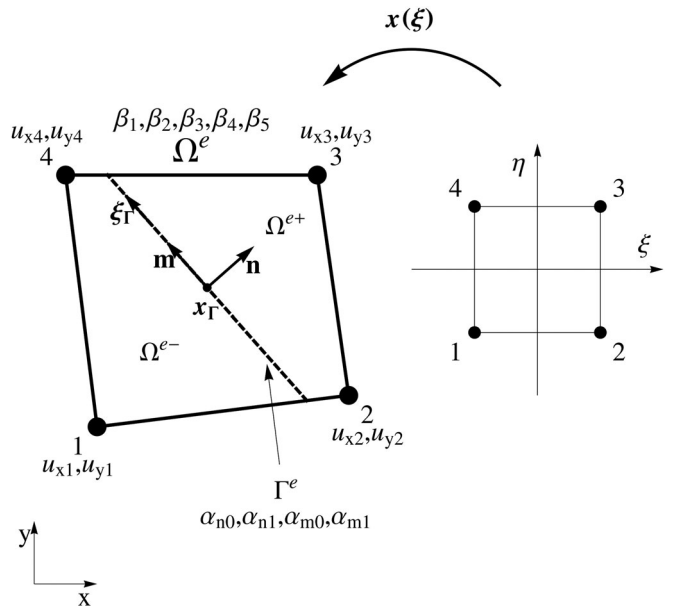


Figure 1. A quadrilateral with an embedded discontinuity.

$$\mathbf{p}_2 = H_\Gamma(\mathbf{x}) \hat{\mathbf{I}} \bar{\mathbf{x}} - \sum_{a \in \Omega^{e+}} N_a \hat{\mathbf{I}} \bar{\mathbf{x}}_a, \quad (4)$$

$$\mathbf{p}_3 = \left(H_\Gamma(\mathbf{x}) - \sum_{a \in \Omega^{e+}} N_a \right) \mathbf{m}, \quad (5)$$

$$\mathbf{p}_4 = \left(H_\Gamma(\mathbf{x}) (\mathbf{m} \cdot \bar{\mathbf{x}}) - \sum_{a \in \Omega^{e+}} N_a (\mathbf{m} \cdot \bar{\mathbf{x}}_a) \right) \mathbf{m}, \quad (6)$$

$$H_\Gamma(\mathbf{x}) = \begin{cases} 1 & \text{for } \mathbf{x} \in \Omega^{e+} \\ 0 & \text{otherwise} \end{cases}, \quad \hat{\mathbf{I}} = \begin{bmatrix} 0 & 1 \\ -1 & 0 \end{bmatrix}. \quad (7)$$

Here, $\mathbf{n} = [n_x, n_y]^T$ and $\mathbf{m} = [m_x, m_y]^T = [-n_y, n_x]^T$ are unit vectors, normal and parallel to the line Γ^e , $\bar{\mathbf{x}} = \mathbf{x} - \mathbf{x}_\Gamma$, $\bar{\mathbf{x}}_a = \mathbf{x}_a - \mathbf{x}_\Gamma$, and \mathbf{x}_Γ are coordinates of the mid-point of Γ^e . The idea behind derivation of (3)-(6) is the following. When the cohesive tractions at the discontinuity are zero, Ω^{e+} should be able to: (i) translate as a rigid body along \mathbf{n} and \mathbf{m} , and (ii) rotate as a rigid body around \mathbf{x}_Γ , all without affecting Ω^{e-} . Additionally, Ω^{e+} should be able to (iii) stretch along \mathbf{m} without affecting Ω^{e-} at zero cohesive tractions.

The components of the strain tensor are

$$\epsilon = \left[\frac{\partial u_x}{\partial x}, \frac{\partial u_y}{\partial y}, \frac{\partial u_x}{\partial y} + \frac{\partial u_y}{\partial x} \right]^T = \sum_{a=1}^4 \mathbf{B}_a \mathbf{d}_a^e + \sum_{m=1}^4 \mathbf{G}_m \alpha_m, \quad (8)$$

where the matrices contain the derivatives of the interpolation functions as:

$$\mathbf{B}_a = \left[\left[\frac{\partial N_a}{\partial x}, 0, \frac{\partial N_a}{\partial y} \right]^T, \left[0, \frac{\partial N_a}{\partial y}, \frac{\partial N_a}{\partial x} \right]^T \right], \quad (9)$$

$$\mathbf{G}_1 = - \underbrace{\sum_{a \in \Omega^{e+}} \mathbf{B}_a \mathbf{n}}_{\bar{\mathbf{G}}_1} + \underbrace{\delta_\Gamma(\mathbf{x}) \mathbf{B}_n \mathbf{n}}_{\bar{\mathbf{G}}_1}, \quad (10)$$

$$\mathbf{G}_2 = - \underbrace{\sum_{a \in \Omega^{e+}} \mathbf{B}_a \hat{\mathbf{I}} \bar{\mathbf{x}}_a}_{\bar{\mathbf{G}}_2} + \underbrace{\delta_\Gamma((\mathbf{x}) \mathbf{B}_n \mathbf{n} \xi_\Gamma(\mathbf{x}) - \mathbf{B}_n \mathbf{m} (\mathbf{n} \cdot \bar{\mathbf{x}}))}_{\bar{\mathbf{G}}_2}, \quad (11)$$

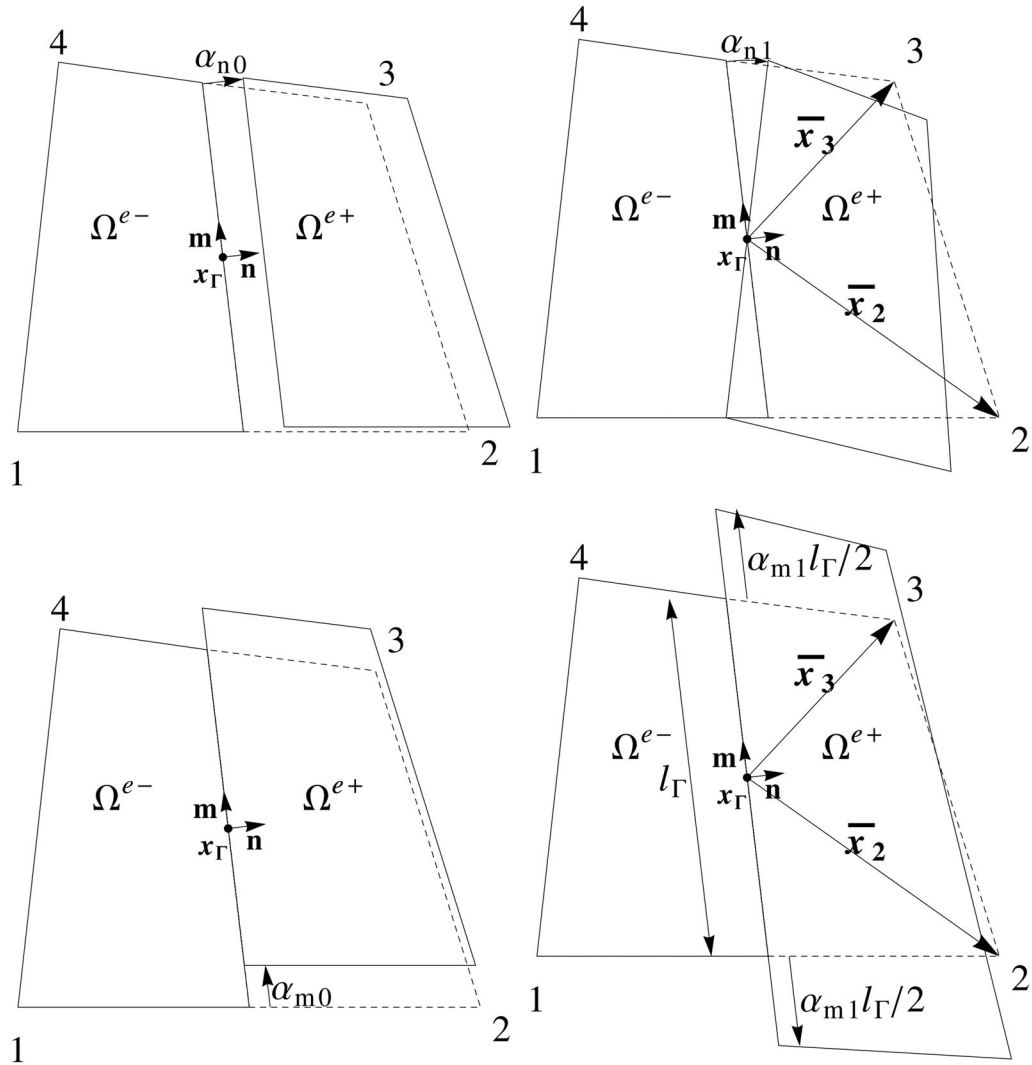


Figure 2. The separation modes.

$$\mathbf{G}_3 = - \underbrace{\sum_{a \in \Omega^{e+}} \mathbf{B}_a \mathbf{m}}_{\overline{\mathbf{G}}_3} + \underbrace{\delta_\Gamma(\mathbf{x}) \mathbf{B}_n \mathbf{m}}_{\overline{\overline{\mathbf{G}}}_3}, \quad (12)$$

$$\mathbf{G}_4 = \underbrace{H_\Gamma(\mathbf{x}) \mathbf{B}_m \mathbf{m}}_{\overline{\mathbf{G}}_4} - \sum_{a \in \Omega^{e+}} \mathbf{B}_a (\mathbf{m} \cdot \overline{\mathbf{x}}_a) \mathbf{m} + \underbrace{\delta_\Gamma(\mathbf{x}) \mathbf{B}_n \mathbf{m} \xi_\Gamma(\mathbf{x})}_{\overline{\overline{\mathbf{G}}}_4}, \quad (13)$$

with the following notation used:

$$\delta_\Gamma(\mathbf{x}) = \begin{cases} \infty & \text{for } \mathbf{x} \in \Gamma^e \\ 0 & \text{otherwise} \end{cases}, \quad \mathbf{B}_n = \begin{bmatrix} [n_x, 0, n_y]^T, & [0, n_y, n_x]^T \end{bmatrix},$$

$$\mathbf{B}_m = \begin{bmatrix} [m_x, 0, m_y]^T, & [0, m_y, m_x]^T \end{bmatrix}.$$

Here, $\xi_\Gamma \in [-l_\Gamma/2, l_\Gamma/2]$ is a coordinate along Γ^e (with origin at \mathbf{x}_Γ and direction of \mathbf{m}) and l_Γ is the length of discontinuity. Vectors \mathbf{G}_m are derivatives of \mathbf{p}_m with respect to x and y , see [33] for details. Each of them consists of two parts: the bounded one (marked with one-bar superscript) and the unbounded one (marked with two-bars superscript) with the Dirac-delta distribution δ_Γ , see (10)-(13). With this

in mind, we divide the strains into the bounded (regular) part $\overline{\epsilon}$ and the unbounded (singular) part $\overline{\overline{\epsilon}}$ as:

$$\epsilon = \underbrace{\sum_{a,m=1}^4 \mathbf{B}_a d_a^e}_{\overline{\epsilon}} + \overline{\mathbf{G}}_m \alpha_m + \sum_{m=1}^4 \underbrace{\overline{\overline{\mathbf{G}}}_m \alpha_m}_{\overline{\overline{\epsilon}}}. \quad (14)$$

2.2. Elasto-plasticity for the bulk

We model the material at the bulk material point by the J_2 plane stress elasto-plasticity with isotropic hardening, see e.g. [34]. With $\overline{W}^*(\boldsymbol{\sigma})$ denoting the complementary strain energy, the strain energy is defined as, see e.g. [35]:

$$\overline{W}(\overline{\epsilon} - \overline{\epsilon}^p) = \boldsymbol{\sigma}^T (\overline{\epsilon} - \overline{\epsilon}^p) - \overline{W}^*(\boldsymbol{\sigma}), \quad (15)$$

where $\overline{\epsilon}$ are regular strains and $\overline{\epsilon}^p$ are (regular) plastic strains. The free energy at the bulk's material point is sum of the strain energy \overline{W} and the hardening potential $\overline{\Xi}$:

$$\overline{\Psi}(\overline{\epsilon} - \overline{\epsilon}^p, \overline{\xi}) = \overline{W}(\overline{\epsilon} - \overline{\epsilon}^p) + \overline{\Xi}(\overline{\xi}), \quad (16)$$

where $\overline{\xi} \geq 0$ is the strain-like hardening variable. The mechanical dissipation pseudo-time rate is (see e.g. [34] for details of definition):

$$0 \leq \bar{D} \stackrel{\text{def.}}{=} \boldsymbol{\sigma}^T \dot{\bar{\boldsymbol{\epsilon}}} - \dot{\bar{\Psi}} \stackrel{(16)}{=} \boldsymbol{\sigma}^T \dot{\bar{\boldsymbol{\epsilon}}}^p - \dot{\boldsymbol{\sigma}}^T (\bar{\boldsymbol{\epsilon}} - \bar{\boldsymbol{\epsilon}}^p) + \left(\frac{\partial \bar{W}^*}{\partial \boldsymbol{\sigma}} \right)^T \dot{\boldsymbol{\sigma}} - \frac{d\bar{\xi}}{d\bar{\xi}} \dot{\bar{\xi}}, \quad (17)$$

where the dot represents derivative with respect to the pseudo-time τ . If $\bar{D} = 0$, we have an elastic case, where the plastic variables do not change, i.e. $\dot{\bar{\boldsymbol{\epsilon}}}^p = \mathbf{0}$, $\dot{\bar{\xi}} = 0$. One can conclude from (17) that such a case yields $\bar{\boldsymbol{\epsilon}} - \bar{\boldsymbol{\epsilon}}^p = \frac{\partial \bar{W}^*}{\partial \boldsymbol{\sigma}}$. By defining the stress-like hardening variable as $\bar{q} = -\frac{d\bar{\xi}}{d\bar{\xi}}$, the pseudo-time rate of plastic dissipation can now be written as

$$0 < \bar{D}^p = \boldsymbol{\sigma}^T \dot{\bar{\boldsymbol{\epsilon}}}^p + \bar{q} \dot{\bar{\xi}}. \quad (18)$$

In what follows, we will use the simplest form of the complementary strain energy $\bar{W}^*(\boldsymbol{\sigma}) = \frac{1}{2} \boldsymbol{\sigma}^T \mathbf{C}^{-1} \boldsymbol{\sigma}$, with

$$\mathbf{C} = \frac{E}{1-\nu^2} \begin{bmatrix} [1, \nu, 0]^T & [\nu, 1, 0]^T & [0, 0, \frac{1-\nu}{2}]^T \end{bmatrix}, \quad (19)$$

where \mathbf{C} is chosen for the plane-stress state (in view of the numerical examples presented below), E is elastic modulus, and ν is Poisson's ratio. The von Mises yield function will be used in the yield criterion. The latter can be written as

$$\bar{\phi}(\boldsymbol{\sigma}, \bar{q}) = \boldsymbol{\sigma}^T \mathbf{A} \boldsymbol{\sigma} - \left(1 - \frac{\bar{q}}{\sigma_y} \right)^2 \leq 0, \quad (20)$$

where σ_y is the uniaxial yield stress, and \mathbf{A} equals (for the plane stress)

$$\mathbf{A} = \frac{1}{2\sigma_y^2} \begin{bmatrix} [2, -1, 0]^T & [-1, 2, 0]^T & [0, 0, 6]^T \end{bmatrix}. \quad (21)$$

By using (18) at enforcing the principal of the maximum plastic dissipation, and taking simultaneously into account the constraint on stresses (20) (see e.g. [34]), the evolution equations for the internal variables follow as, see e.g. [33]:

$$\dot{\bar{\boldsymbol{\epsilon}}}^p = \dot{\bar{\gamma}} \frac{\partial \bar{\phi}}{\partial \boldsymbol{\sigma}} = \dot{\bar{\gamma}} 2 \mathbf{A} \boldsymbol{\sigma}, \quad (22)$$

$$\dot{\bar{\xi}} = \dot{\bar{\gamma}} \frac{\partial \bar{\phi}}{\partial \bar{q}} = \dot{\bar{\gamma}} \frac{2}{\sigma_y} \left(1 - \frac{\bar{q}}{\sigma_y} \right) = \dot{\bar{\gamma}} \frac{2}{\sigma_y} \sqrt{\boldsymbol{\sigma}^T \mathbf{A} \boldsymbol{\sigma}}, \quad (23)$$

where $\dot{\bar{\gamma}} \geq 0$ plays the role of the plastic multiplier. The Kuhn-Tucker loading/unloading conditions, and the consistency condition, also apply: $\dot{\bar{\gamma}} \geq 0$, $\bar{\phi} \leq 0$, $\dot{\bar{\gamma}} \bar{\phi} = 0$, $\dot{\bar{\gamma}} \dot{\bar{\phi}} = 0$.

2.3. Softening plasticity for the discontinuity

We model cohesion degradation in the discontinuity point with softening plasticity. It is governed by the failure criterion (with the proposal for failure function $\bar{\phi}$ left open at the moment)

$$\bar{\phi} = \bar{\phi}(\mathbf{t}, \bar{q}) \leq 0, \quad (24)$$

where $\mathbf{t} = [t_n, t_m]^T$ are tractions, $\bar{q}(\bar{\xi})$ is traction-like softening variable, and $\bar{\xi} \geq 0$ is separation-like softening variable. Only plastic deformations, which are equal to the displacement-jumps $\bar{\mathbf{u}} = [\bar{\mathbf{u}}_n, \bar{\mathbf{u}}_m]^T$ (see Figure 3), take place at the discontinuity. The components of $\bar{\mathbf{u}}$ are expressed as

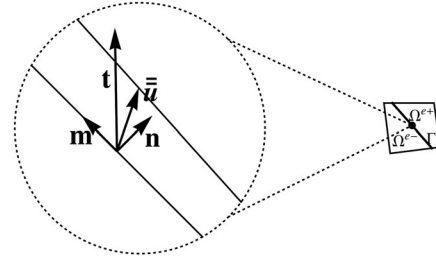


Figure 3. A point at the discontinuity Γ^e .

$$\bar{\mathbf{u}}_n(\zeta_\Gamma) = \alpha_1 + \zeta_\Gamma \alpha_2, \quad \bar{\mathbf{u}}_m(\zeta_\Gamma) = \alpha_3 + \zeta_\Gamma \alpha_4. \quad (25)$$

By considering associative plasticity and the principal of maximum plastic dissipation (see e.g. [34]), we can obtain, after a short derivation (see [33, 36]), the following evolution equations

$$\dot{\bar{\mathbf{u}}} = \dot{\bar{\gamma}} \frac{\partial \bar{\phi}}{\partial \mathbf{t}}, \quad \dot{\bar{\xi}} = \dot{\bar{\gamma}} \frac{\partial \bar{\phi}}{\partial \bar{q}}, \quad (26)$$

where $\dot{\bar{\gamma}} \geq 0$ is the plastic multiplier. The Kuhn-Tucker loading/unloading conditions and the consistency condition also apply: $\dot{\bar{\gamma}} \geq 0$, $\bar{\phi} \leq 0$, $\dot{\bar{\gamma}} \bar{\phi} = 0$, $\dot{\bar{\gamma}} \dot{\bar{\phi}} = 0$.

2.4. Hellinger-Reissner functional

We will obtain the element's governing equations from the Hellinger-Reissner functional (see e.g. [34]) that has for the ED formulation the following form

$$\begin{aligned} \Pi^e(\mathbf{u}, \boldsymbol{\alpha}^e, \boldsymbol{\sigma}) &= t^e \int_{\Omega^e} \boldsymbol{\sigma}^T (\bar{\boldsymbol{\epsilon}}(\mathbf{u}, \boldsymbol{\alpha}^e) - \bar{\boldsymbol{\epsilon}}^p) d\Omega \\ &\quad - \frac{1}{2} t^e \int_{\Omega^e} \boldsymbol{\sigma}^T \mathbf{C}^{-1} \boldsymbol{\sigma} d\Omega - \Pi^{\text{ext}, e}(\mathbf{u}). \end{aligned} \quad (27)$$

It treats the displacements \mathbf{u} , additional kinematic parameters $\boldsymbol{\alpha}^e = [\alpha_1, \alpha_2, \alpha_3, \alpha_4]^T$, and stresses $\boldsymbol{\sigma}$ as independent variables. Here, t^e is element thickness, and $\Pi^{\text{ext}, e}$ is potential of element's external forces. We note that only the regular (i.e. bounded) elastic strains $\bar{\boldsymbol{\epsilon}} - \bar{\boldsymbol{\epsilon}}^p$ enter the functional (27). The stationary conditions of the above potential are determined by setting to zero its variation. When performed, the following element's governing equations are obtained

$$G_u^e = t^e \underbrace{\int_{\Omega^e} \hat{\boldsymbol{\epsilon}}^T \boldsymbol{\sigma} d\Omega}_{G_u^{\text{int}, e}} - G_u^{\text{ext}, e} = 0, \quad (28)$$

$$G_\sigma^e = t^e \int_{\Omega^e} \hat{\boldsymbol{\sigma}}^T (\bar{\boldsymbol{\epsilon}} - \bar{\boldsymbol{\epsilon}}^p - \mathbf{C}^{-1} \boldsymbol{\sigma}) d\Omega = 0. \quad (29)$$

Here, $G_u^{\text{ext}, e}(\hat{\mathbf{u}})$ is variation of $\Pi^{\text{ext}, e}(\mathbf{u})$, and $\hat{\mathbf{u}}, \hat{\boldsymbol{\sigma}}, \hat{\boldsymbol{\epsilon}} = \hat{\boldsymbol{\epsilon}}(\hat{\mathbf{u}}, \hat{\boldsymbol{\alpha}}^e, \mathbf{u})$ denote variations of \mathbf{u} , $\boldsymbol{\sigma}$ and $\bar{\boldsymbol{\epsilon}}(\mathbf{u}, \boldsymbol{\alpha}^e)$, respectively.

2.5. Interpolation of stresses

The Hellinger-Reissner functional calls for interpolation of the stresses over the element. We apply the following interpolation

$$\boldsymbol{\sigma} = [\sigma_{xx}, \sigma_{yy}, \sigma_{xy}]^T = \mathbf{S}\boldsymbol{\beta}^e, \quad (30)$$

where $\boldsymbol{\beta}^e = [\beta_1, \beta_2, \beta_3, \beta_4, \beta_5]^T$ is vector of stress parameters and \mathbf{S} is matrix of the stress interpolation functions proposed by Pian and Sumihara (see e.g. [27]). It has the following form:

$$\mathbf{S} = \begin{bmatrix} 1 & 0 & 0 & j_{11}^2 \eta & j_{12}^2 \xi \\ 0 & 1 & 0 & j_{21}^2 \eta & j_{22}^2 \xi \\ 0 & 0 & 1 & j_{11} j_{21} \eta & j_{12} j_{22} \xi \end{bmatrix}. \quad (31)$$

where $j_{ij}(i, j = 1, 2)$ are components of the Jacobian matrix evaluated at element's center. They are taking the role in transformation of stresses from ξ coordinates, where the stress interpolations are primarily defined, to x coordinates. This transformation needs to be performed at element's center in order to enable description of a constant stress state over the element, see e.g. [37].

2.6. Interpolation of variations

In the spirit of the Petrov-Galerkin finite element approximation, that provides optimal embedded discontinuity finite element formulations, see [6], we interpolate the variations of strains $\hat{\boldsymbol{\epsilon}}$ (28) in a different manner than the interpolations of real strains $\bar{\boldsymbol{\epsilon}}$ (14). The following interpolation is chosen for $\hat{\boldsymbol{\epsilon}}$:

$$\hat{\boldsymbol{\epsilon}} = \sum_{a,m=1}^4 \mathbf{B}_a \hat{\mathbf{d}}_a^e + \hat{\mathbf{G}}_m \hat{\alpha}_m, \quad (32)$$

where $\hat{\mathbf{d}}_a^e$ and $\hat{\alpha}_m$ are variations of nodal displacements and the discontinuity parameters. More importantly, $\hat{\mathbf{G}}_m$ is a modified \mathbf{G}_m operator that is computed as (the average of \mathbf{G}_m is deduced from \mathbf{G}_m):

$$\hat{\mathbf{G}}_m = \mathbf{G}_m - \frac{1}{A_{\Omega^e}} \int_{\Omega^e} \mathbf{G}_m d\Omega, \quad \int_{\Omega^e} \hat{\mathbf{G}}_m d\Omega = \mathbf{0}, \quad (33)$$

where A_{Ω^e} is element's area. We note that the constraint (33)₂ is necessary if the local equilibrium equations (derived below, see Eq. (40)) are to hold for a constant $\boldsymbol{\sigma}$. Because \mathbf{G}_m and consequently $\hat{\mathbf{G}}_m$ operators have bounded and unbounded parts, the virtual strains (32) share the same feature. Therefore, the bounded and unbounded virtual strains enter the stationary condition (28).

The variations of the stresses are interpolated over the element in the same manner as the real stresses:

$$\hat{\boldsymbol{\sigma}} = \mathbf{S}\hat{\boldsymbol{\beta}}^e, \quad (34)$$

where $\hat{\boldsymbol{\beta}}^e$ are virtual stress parameters. The virtual displacements are also interpolated in the same manner as real displacements (2). Because of the assumption that the parameters of the displacement-jumps are not associated with the external loading, $G_u^{ext,e}$ in (28) depends only on nodal virtual displacements.

2.7. Stationary condition equations

In this section, we elaborate on the stationary condition equations (28) and (29), and we introduce tractions at the discontinuity.

2.7.1. Equation (37)

By using interpolations (30) and (32), we can rewrite (28) as:

$$\begin{aligned} G_u^e &= \underbrace{\sum_{a=1}^4 \int_{\Omega^e \setminus \Gamma^e} t^e \hat{\mathbf{d}}_a^{e,T} \mathbf{B}_a^T \mathbf{S} \boldsymbol{\beta}^e d\Omega}_{G_{u,d}^{int,e}} - G_u^{ext,e} \\ &+ \underbrace{\sum_{m=1}^4 \int_{\Omega^e} t^e \hat{\alpha}_m \hat{\mathbf{G}}_m^T \mathbf{S} \boldsymbol{\beta}^e d\Omega}_{G_{u,\alpha}^{int,e}} = 0, \quad \forall \hat{\mathbf{d}}_a^e, \forall \hat{\alpha}_m \end{aligned} \quad (35)$$

or, in a compact form:

$$G_u^e = \underbrace{(G_{u,d}^{int,e} - G_u^{ext,e})}_{=0} + \underbrace{G_{u,\alpha}^{int,e}}_{=0} = 0. \quad (36)$$

As indicated in (36), two equations need to be considered. Let us write $G_{u,d}^{int,e}$ by vectors of element's internal nodal forces and virtual nodal displacements:

$$\begin{aligned} \mathbf{f}_d^{int,e} &= [\mathbf{f}_{a,d}^{int,e,T}]^T, \\ \mathbf{f}_{a,d}^{int,e} &= t^e \int_{\Omega^e \setminus \Gamma^e} \mathbf{B}_a^T \mathbf{S} \boldsymbol{\beta}^e d\Omega \Rightarrow G_{u,d}^{int,e} = \hat{\mathbf{d}}_a^{e,T} \mathbf{f}_d^{int,e}, \end{aligned} \quad (37)$$

where $\hat{\mathbf{d}}_a^e = [\hat{\mathbf{d}}_a^{e,T}]^T$. In a similar manner, we can write $G_u^{ext,e}$ as:

$$G_u^{ext,e} = \sum_{a=1}^4 \hat{\mathbf{d}}_a^{e,T} \mathbf{f}_{a,d}^{ext,e} = \hat{\mathbf{d}}^T \mathbf{f}_d^{ext,e}, \quad \mathbf{f}_d^{ext,e} = [\mathbf{f}_{a,d}^{ext,e,T}]^T, \quad (38)$$

where $\mathbf{f}_{a,d}^{ext,e}$ is vector of element's external nodal forces. Because $\hat{\mathbf{d}}$ is arbitrary, the first equation from (36) yields the following system of equations in notation from (37) and (38):

$$\hat{\mathbf{d}}^{e,T} (\mathbf{f}_d^{int,e} - \mathbf{f}_d^{ext,e}) = 0 \Rightarrow \mathbf{f}_d^{int,e} - \mathbf{f}_d^{ext,e} = \mathbf{f}_d^e = \mathbf{0}, \quad (39)$$

representing element's equilibrium between internal and external nodal forces.

Let us now turn to the second equation from (36). Since $\hat{\alpha}_m$ are arbitrary, the corresponding integrals should be zero, i.e.

$$\hat{\alpha}_m \int_{\Omega^e} \underbrace{t^e \hat{\mathbf{G}}_m^T \mathbf{S} \boldsymbol{\beta}^e d\Omega}_{=0} = 0, \quad m = 1, \dots, 4. \quad (40)$$

It is obvious from (40) that the equation can hold for a constant stress state only if (33)₂ is fulfilled. Recall that $\hat{\mathbf{G}}_m$ consists of regular and singular parts that will be denoted as $\overline{\hat{\mathbf{G}}}_m$ and $\overline{\hat{\mathbf{G}}}_m$ (see Appendix A for details). With this in mind, we introduce the following notation for the integral from (40):

$$t^e \int_{\Omega^e} \hat{\mathbf{G}}_m^T \mathbf{S} \boldsymbol{\beta}^e d\Omega = f_{m,\alpha}^{\Omega^e} + f_{m,\alpha}^{\Gamma^e} = f_{m,\alpha}^e = 0, \quad m = 1, \dots, 4, \quad (41)$$

where $f_{m,\alpha}^{\Omega^e}$ relates to the regular part of $\hat{\mathbf{G}}_m$ as (see Appendix B):

$$f_{m,\alpha}^{\Omega^e} = t^e \int_{\Omega^e \setminus \Gamma^e} \bar{\mathbf{G}}_m^T \mathbf{S} \boldsymbol{\beta}^e d\Omega, \quad (42)$$

and $f_{m,\alpha}^{\Gamma^e}$ relates to the singular part of $\hat{\mathbf{G}}_m$ as (see Appendix B):

$$f_{1,\alpha}^{\Gamma^e} = t^e \int_{\Gamma^e} t_n d\Gamma, \quad f_{2,\alpha}^{\Gamma^e} = t^e \int_{\Gamma^e} \xi_{\Gamma} t_n d\Gamma, \quad (43)$$

$$f_{3,\alpha}^{\Gamma^e} = t^e \int_{\Gamma^e} t_m d\Gamma, \quad f_{4,\alpha}^{\Gamma^e} = t^e \int_{\Gamma^e} \xi_{\Gamma} t_m d\Gamma. \quad (44)$$

Here, t_n and t_m are normal and tangential tractions at discontinuity. By collecting eqs. (41)-(44) in vector form, we have:

$$\mathbf{f}_{\alpha}^{\Omega^e} + \mathbf{f}_{\alpha}^{\Gamma^e} = \left[f_{m,\alpha}^{\Omega^e} \right]^T + \left[f_{m,\alpha}^{\Gamma^e} \right]^T = \mathbf{f}_{\alpha}^e = \mathbf{0}. \quad (45)$$

Eqs. (45) are again the equilibrium equations: they enforce the weak equilibrium between the stresses in the bulk and the tractions at discontinuity.

2.7.2. Equation (18)

By using interpolations (14), (30) and (34) in equation (29), one gets $\mathbf{G}_{\alpha}^e = \hat{\boldsymbol{\beta}}^{e,T} \mathbf{f}_{\beta}^e = \mathbf{0}$, and (since $\hat{\boldsymbol{\beta}}$ is arbitrary):

$$\mathbf{f}_{\beta}^e = t^e \int_{\Omega^e / \Gamma^e} \mathbf{S}^T \left(\sum_{a=1}^4 \mathbf{B}_a \mathbf{d}_a^e + \sum_{m=1}^4 \bar{\mathbf{G}}_m \alpha_m - \bar{\boldsymbol{\epsilon}}^p - \mathbf{C}^{-1} \mathbf{S} \boldsymbol{\beta}^e \right) d\Omega = \mathbf{0}. \quad (46)$$

This equation represents an approximation of the weak form of the kinematic compatibility equation.

2.7.3. Resulting sets of nonlinear equations

Two stationary conditions of the functional, (28) and (29), thus result in three sets of nonlinear equations of the element, which are to be solved after application of the finite element assembly procedure for the mesh of the elements. Those three sets are:

$$\mathbf{f}_d^e(\boldsymbol{\beta}^e) \stackrel{(39)}{=} \mathbf{f}_d^{int,e}(\boldsymbol{\beta}^e) - \mathbf{f}_d^{ext,e} = \mathbf{0}, \quad (47)$$

$$\mathbf{f}_{\alpha}^e(\boldsymbol{\beta}^e, \boldsymbol{\alpha}^e) \stackrel{(45)}{=} \mathbf{f}_{\alpha}^{\Omega^e}(\boldsymbol{\beta}^e) + \mathbf{f}_{\alpha}^{\Gamma^e}(\boldsymbol{\alpha}^e) = \mathbf{0}, \quad (48)$$

$$\mathbf{f}_{\beta}^e(\mathbf{d}_a^e, \boldsymbol{\beta}^e, \boldsymbol{\alpha}^e) \stackrel{(46)}{=} \mathbf{0}. \quad (49)$$

The nodal displacements \mathbf{d}_a^e , the element's stress parameters $\boldsymbol{\beta}^e$, and the element's discontinuity parameters $\boldsymbol{\alpha}^e$ are unknowns in the above equations (along with the internal variables of inelastic constitutive models).

We use the 2×2 Gauss integration scheme in order to evaluate the area integrals that appear in Eqs. (39), (45) and (46). The 2-point Gauss integration scheme is used to evaluate the line integrals that appear in Eq. (45). The internal variables of the presented finite element formulation are plastic strains and strain-like hardening variable $\bar{\boldsymbol{\epsilon}}^p$ and $\bar{\xi}$ at integration points of the bulk, and displacement-like softening variable $\bar{\xi}$ at integration points of discontinuity.

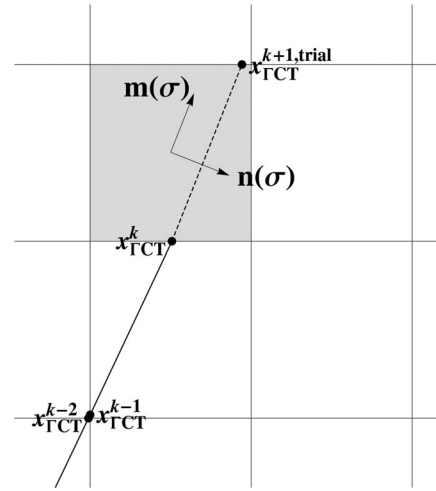


Figure 4. The slip line extension.

2.8. Tracking slip line across the mesh

For a non-cracked element, Eq. (45) does not exist, and in Eq. (46) $\boldsymbol{\alpha}^e = \mathbf{0}$. The discontinuity embedding changes considerable element equations, and only Eq. (39) remains the same for cracked and non-cracked elements. If such changes of equations are too many in a single solution increment (i.e. if a considerable number of elements indicate slip line embedding), the convergence may be lost in that increment. Even if the convergence is not lost, the obtained solution in general shows locking, unless the solution computation is combined with tracking a single slip line across the mesh. Therefore, we allow in this work for a single slip line propagation across the mesh (or a predefined domain of the mesh). Moreover, we demand that the slip line extends at most by one element in one load increment (in Figure 4 such element is gray). This very simple approach can work relatively well (with a small error in solution) only if the load increments are very small. For a better crack tracking algorithm, we refer e.g. to [38].

According to [39], the orientation of the propagation of the slip line at the material failure point for 2d plane stress J_2 elasto-plasticity is defined as:

$$\tan^2(\Theta_{cr}) = -\frac{\tilde{\sigma}_{xx} + \tilde{\sigma}_{yy} + A}{\tilde{\sigma}_{xx} + \tilde{\sigma}_{yy} - A} \geq 0, \quad (50)$$

$$A = 3\sqrt{\tilde{\sigma}_{xx}^2 + 4\tilde{\sigma}_{xy}^2 - 2\tilde{\sigma}_{xx}\tilde{\sigma}_{yy} + \tilde{\sigma}_{xx}^2}, \quad (51)$$

where Θ_{cr} is the angle between the minimum principal stress $\tilde{\sigma}_2$ and tangent to the existing slip line at its current tip $x_{\Gamma CT}^k$. The expression (50) is used in order to compute the orientation of the extension of the slip line across the gray element. As for the stresses utilized in (50), we choose those from the gray element middle point, i.e. $\bar{\boldsymbol{\sigma}} = \boldsymbol{\sigma}|_{\xi=0, \eta=0}$. This enables computation of unit vectors of the discontinuity, \mathbf{n} and \mathbf{m} , as $\mathbf{n} = \mathbf{n}(\bar{\boldsymbol{\sigma}})$ and $\mathbf{m} = \mathbf{m}(\bar{\boldsymbol{\sigma}})$, where \mathbf{m} is defined by Θ_{cr} , and \mathbf{n} is perpendicular to \mathbf{m} . Once the discontinuity direction in the gray element is determined, the trial point of the new tip of the slip line, denoted as $x_{\Gamma CT}^{k+1, trial}$ on Figure 4, is known. This trial point can be fixed only after checking if discontinuity in the gray element is feasible.

If the material failure is predicted (i.e. if $\overline{\phi} > 0$ holds) at both Gauss integration points on the discontinuity Γ^e of the gray element, the discontinuity is embedded and the new tip of the slip line is $\mathbf{x}_{\text{GCT}}^{k+1} = \mathbf{x}_{\text{GCT}}^{k+1, \text{trial}}$. Otherwise, the discontinuity is not embedded.

3. Computational and implementation aspects

In this section, we will show how the nonlinear equations (39), (45) and (46) are solved. The solution is searched for at the discrete pseudo-time values $0, \tau_1, \tau_2, \dots, \tau_{n-1}, \tau_n, \tau_{n+1}, \dots, T$ by means of the incremental-iterative Newton scheme.

3.1. Computational procedure

Let us consider a typical pseudo-time increment from τ_n to τ_{n+1} . Nodal displacements, stresses, discontinuity parameters and internal variables are given data for each element of the mesh at pseudo-time τ_n , i.e.

$$\text{given : } \mathbf{d}_n^e = \left[\mathbf{d}_{a,n}^e \right]^T, \boldsymbol{\beta}_n^e, \boldsymbol{\alpha}_n^e, \overline{\boldsymbol{\epsilon}}_n^{p,b}, \overline{\boldsymbol{\zeta}}_n^b, \overline{\boldsymbol{\zeta}}_n^g, \quad e = 1, 2, \dots, N_{el}, \quad (52)$$

where $(\circ)_n$ denotes value of (\circ) at τ_n . The $b = 1, 2, 3, 4$ denotes the bulk integration points and $g = 1, 2$ the discontinuity integration points. We will iterate in order to compute converged values at τ_{n+1} , i.e.

$$\text{find : } \mathbf{d}_{n+1}^e, \boldsymbol{\beta}_{n+1}^e, \boldsymbol{\alpha}_{n+1}^e, \overline{\boldsymbol{\epsilon}}_{n+1}^{p,b}, \overline{\boldsymbol{\zeta}}_{n+1}^b, \overline{\boldsymbol{\zeta}}_{n+1}^g. \quad (53)$$

The iteration counter will be denoted as i . The iterative computation is split into two phases, because the stationary point equations can be computed separately from the internal variables, see e.g. [34]. We first compute iterative changes of nodal displacements, stress parameters and discontinuity parameters, and perform their update as:

$$\mathbf{d}_{n+1}^{e,i} = \mathbf{d}_{n+1}^{e,i-1} + \Delta \mathbf{d}_{n+1}^{e,i}. \quad (54)$$

$$\boldsymbol{\beta}_{n+1}^{e,i} = \boldsymbol{\beta}_{n+1}^{e,i-1} + \Delta \boldsymbol{\beta}_{n+1}^{e,i}, \quad \boldsymbol{\alpha}_{n+1}^{e,i} = \boldsymbol{\alpha}_{n+1}^{e,i-1} + \Delta \boldsymbol{\alpha}_{n+1}^{e,i}. \quad (55)$$

In the second phase, we immediately use the results of the first phase and compute iterative values of internal variables of the bulk and discontinuity: $\overline{\boldsymbol{\epsilon}}_{n+1}^{p,b,i}, \overline{\boldsymbol{\zeta}}_{n+1}^{b,i}, \overline{\boldsymbol{\zeta}}_{n+1}^{g,i}$ (we will omit index b in what follows, in particular, in Section 3.3) The iterations for the values at τ_{n+1} are completed when a predefined convergence tolerance is reached.

3.2. Displacement, stress and discontinuity parameters

The iterative change of nodal displacements $\Delta \mathbf{d}_{n+1}^{e,i}$ in (54) is determined by solving the global (mesh related) system of equations

$$\mathbb{A}_{e=1}^{N_{el}} \left(\mathbf{K}_{n+1}^{e,i} \Delta \mathbf{d}_{n+1}^{e,i} \right) = \mathbb{A}_{e=1}^{N_{el}} \left(\mathbf{f}_{n+1}^{e,i} \right), \quad (56)$$

where \mathbb{A} is the finite element assembly operator, $\mathbf{K}_{n+1}^{e,i}$ is element's contribution to the stiffness matrix, and $\mathbf{f}_{n+1}^{e,i}$ is element's contribution to the residual vector. How $\mathbf{K}_{n+1}^{e,i}$ and

$\mathbf{f}_{n+1}^{e,i}$ are obtained is described below in the next two sections.

3.2.1. Element stiffness matrix

The element consistent tangent stiffness matrix and the residual vector are obtained by linearization of (39), (45) and (46) around the last known values of nodal and element parameters, i.e. $\mathbf{d}_{n+1}^{e,i-1}, \boldsymbol{\beta}_{n+1}^{e,i-1}$ and $\boldsymbol{\alpha}_{n+1}^{e,i-1}$. Let us write linearized eqs. (39), (45), and (46) as

$$\begin{bmatrix} \mathbf{K}_{dd} & \mathbf{K}_{d\beta} & \mathbf{K}_{d\alpha} \\ \mathbf{K}_{\beta d} & \mathbf{K}_{\beta\beta} & \mathbf{K}_{\beta\alpha} \\ \mathbf{K}_{\alpha d} & \mathbf{K}_{\alpha\beta} & \mathbf{K}_{\alpha\alpha} \end{bmatrix}_{n+1}^{e,i} \begin{pmatrix} \Delta \mathbf{d} \\ \Delta \boldsymbol{\beta} \\ \Delta \boldsymbol{\alpha} \end{pmatrix}_{n+1}^{e,i} = \begin{pmatrix} -\mathbf{f}_d \\ -\mathbf{f}_\beta \\ -\mathbf{f}_\alpha \end{pmatrix}_{n+1}^{e,i}, \quad (57)$$

where parts of the element's tangent stiffness matrix are:

$$\begin{aligned} \mathbf{K}_{dd,n+1}^{e,i} &= \left(\frac{\partial \mathbf{f}_d}{\partial \mathbf{d}} \right)_{n+1}^{e,i}, \quad \mathbf{K}_{d\beta,n+1}^{e,i} = \left(\frac{\partial \mathbf{f}_d}{\partial \boldsymbol{\beta}} \right)_{n+1}^{e,i}, \quad \mathbf{K}_{d\alpha,n+1}^{e,i} = \left(\frac{\partial \mathbf{f}_d}{\partial \boldsymbol{\alpha}} \right)_{n+1}^{e,i}, \\ \mathbf{K}_{\beta d,n+1}^{e,i} &= \left(\frac{\partial \mathbf{f}_\beta}{\partial \mathbf{d}} \right)_{n+1}^{e,i}, \quad \mathbf{K}_{\beta\beta,n+1}^{e,i} = \left(\frac{\partial \mathbf{f}_\beta}{\partial \boldsymbol{\beta}} \right)_{n+1}^{e,i}, \quad \mathbf{K}_{\beta\alpha,n+1}^{e,i} = \left(\frac{\partial \mathbf{f}_\beta}{\partial \boldsymbol{\alpha}} \right)_{n+1}^{e,i}, \\ \mathbf{K}_{\alpha d,n+1}^{e,i} &= \left(\frac{\partial \mathbf{f}_\alpha}{\partial \mathbf{d}} \right)_{n+1}^{e,i}, \quad \mathbf{K}_{\alpha\beta,n+1}^{e,i} = \left(\frac{\partial \mathbf{f}_\alpha}{\partial \boldsymbol{\beta}} \right)_{n+1}^{e,i}, \quad \mathbf{K}_{\alpha\alpha,n+1}^{e,i} = \left(\frac{\partial \mathbf{f}_\alpha}{\partial \boldsymbol{\alpha}} \right)_{n+1}^{e,i}. \end{aligned} \quad (58)$$

Explicit expressions are given in Appendix C.

3.2.2. Condensation of stress and discontinuity parameters

In order to separate stress and discontinuity parameters from the displacement parameters, we rewrite (57) as

$$\begin{bmatrix} \mathbf{K}_{dd} & \mathbf{K}_{dh} \\ \mathbf{K}_{hd} & \mathbf{K}_{hh} \end{bmatrix}_{n+1}^{e,i} \begin{pmatrix} \Delta \mathbf{d} \\ \Delta \mathbf{h} \end{pmatrix}_{n+1}^{e,i} = \begin{pmatrix} -\mathbf{f}_d \\ -\mathbf{f}_h \end{pmatrix}_{n+1}^{e,i}, \quad (59)$$

where

$$\begin{aligned} \mathbf{K}_{dh,n+1}^{e,i} &= \begin{bmatrix} \mathbf{K}_{d\beta} & \mathbf{K}_{d\alpha} \end{bmatrix}_{n+1}^{e,i}, \quad \mathbf{K}_{hd,n+1}^{e,i} = \begin{bmatrix} \mathbf{K}_{\beta d} \\ \mathbf{K}_{\alpha d} \end{bmatrix}_{n+1}^{e,i}, \\ \mathbf{K}_{hh,n+1}^{e,i} &= \begin{bmatrix} \mathbf{K}_{\beta\beta} & \mathbf{K}_{\beta\alpha} \\ \mathbf{K}_{\alpha\beta} & \mathbf{K}_{\alpha\alpha} \end{bmatrix}_{n+1}^{e,i}, \end{aligned} \quad (60)$$

$$\Delta \mathbf{h}_{n+1}^{e,i} = \begin{pmatrix} \Delta \boldsymbol{\beta} \\ \Delta \boldsymbol{\alpha} \end{pmatrix}_{n+1}^{e,i}, \quad \mathbf{f}_{h,n+1}^{e,i} = \begin{pmatrix} \mathbf{f}_\beta \\ \mathbf{f}_\alpha \end{pmatrix}_{n+1}^{e,i}. \quad (61)$$

We can perform condensation of $\Delta \mathbf{h}_{n+1}^{e,i}$ from (59) in order to get equation of the form $\mathbf{K}_{n+1}^{e,i} \Delta \mathbf{d}_{n+1}^{e,i} = \mathbf{f}_{n+1}^{e,i}$, see (56). By doing so, the element's contribution to the global stiffness matrix is obtained as

$$\mathbf{K}_{n+1}^{e,i} = \mathbf{K}_{dd,n+1}^{e,i} - \mathbf{K}_{dh,n+1}^{e,i} \left(\mathbf{K}_{hh,n+1}^{e,i} \right)^{-1} \mathbf{K}_{hd,n+1}^{e,i}, \quad (62)$$

and element's contribution to the global residual vector is

$$\mathbf{f}_{n+1}^{e,i} = \mathbf{f}_{d,n+1}^{e,i} - \mathbf{K}_{dh,n+1}^{e,i} \left(\mathbf{K}_{hh,n+1}^{e,i} \right)^{-1} \mathbf{f}_{h,n+1}^{e,i}. \quad (63)$$

$\mathbf{K}_{n+1}^{e,i}$ from (62) and $\mathbf{f}_{n+1}^{e,i}$ from (63) are element's contribution to the global system of equations (56).

3.2.3. Iterative solution

With (62) and (63) for each element of the mesh, one can solve the global system of equations (56) for iterative change of nodal displacements of the finite element mesh. Element's iterative change of nodal displacements $\Delta \mathbf{d}_{n+1}^{e,i}$ can be extracted from that solution in order to compute

$$\Delta \mathbf{h}_{n+1}^{e,i} = - \left(\mathbf{K}_{hh,n+1}^{e,i} \right)^{-1} \left[\mathbf{f}_{h,n+1}^{e,i} + \mathbf{K}_{hd,n+1}^{e,i} \Delta \mathbf{d}_{n+1}^{e,i} \right] \quad (64)$$

from (59). New iterative updates of element nodal displacements, stress parameters and discontinuity parameters can now be obtained by using (54) and (55).

3.2.4. Invertibility of \mathbf{K}_{hh}^e matrix

Computation of (62)-(64) requires inversion of \mathbf{K}_{hh}^e (a 9×9 matrix if all modes from Figure 2 are considered). This matrix is well conditioned in most cases. An exception is when: (i) all modes from Figure 2 are considered, (ii) tractions at discontinuity are zero, and (iii) discontinuity separates a single node from the rest of the element. If this is detected, we replace (45) with

$$\mathbf{f}_{\alpha,\kappa}^e = \mathbf{f}_{\alpha}^e + \kappa [0, (\alpha_{2,n+1} - \alpha_{2,n}), 0, (\alpha_{4,n+1} - \alpha_{4,n})]^T = \mathbf{0}, \quad (65)$$

where $\kappa > 0$ plays a role of the stabilization parameter. This leads to the replacement of matrix in (57) with $\mathbf{K}_{\alpha\alpha,\kappa}^e = \mathbf{K}_{\alpha\alpha}^e + \text{DIAG}[0, \kappa, 0, \kappa]$. The parameter κ should be the smallest number that is large enough to make matrix $\mathbf{K}_{hh,\kappa}^e$ numerically invertible. Our numerical tests suggest the order of 10^{-3} . The introduced stabilization is similar to the one described in [18].

3.3. Internal variables

We can now describe update of the internal variables at the integration points in the second phase of iteration i in pseudo-time step $[\tau_n, \tau_{n+1}]$. From the first phase, we have brought $\mathbf{d}_{n+1}^{e,i}$, $\boldsymbol{\beta}_{n+1}^{e,i}$ and $\boldsymbol{\alpha}_{n+1}^{e,i}$. Therefore, the stress parameters $\boldsymbol{\beta}_{n+1}^{e,i}$ (and thus the bulk stresses) are given and cannot be changed in the second phase.

3.3.1. Bulk

Only the plastic strains and the strain-like hardening variable can be adapted in order to make the stresses admissible (i.e. in accordance with the constitutive equations). The proposed stress-driven procedure, which consists of trial and correction, is suitable for non-zero hardening.

3.3.1.1. Trial-correction procedure. We first compute the current stresses $\boldsymbol{\sigma}_{n+1}^i = \mathbf{S} \boldsymbol{\beta}_{n+1}^{e,i}$, the trial value of the strain-like hardening variable $\bar{\zeta}_{n+1}^{trial,i} = \bar{\zeta}_n$, and the trial value of the yield function $\bar{\phi}_{n+1}^{trial,i}$. If

$$\bar{\phi}_{n+1}^{trial,i} = \bar{\phi}(\boldsymbol{\sigma}_{n+1}^i, \bar{q}(\bar{\zeta}_{n+1}^{trial,i})) \leq 0, \quad (66)$$

the values of internal variables remain unchanged (the step from τ_n to τ_{n+1} is elastic for current iteration): $\bar{\zeta}_{n+1}^i = \bar{\zeta}_n$

and $\bar{\boldsymbol{\epsilon}}_{n+1}^{p,i} = \bar{\boldsymbol{\epsilon}}_n^p$. If (66) does not hold, a correction is performed, because the step from τ_n to τ_{n+1} is plastic for current iteration. We use the backward Euler integration scheme to get discrete version of evolution equations (22) and (23) as:

$$\begin{aligned} \bar{\boldsymbol{\epsilon}}_{n+1}^{p,i} &= \bar{\boldsymbol{\epsilon}}_n^p + \bar{\gamma}_{n+1}^i 2\mathbf{A}\boldsymbol{\sigma}_{n+1}^i, \\ \bar{\zeta}_{n+1}^i &= \bar{\zeta}_n + \bar{\gamma}_{n+1}^i \frac{2}{\sigma_y} \sqrt{(\boldsymbol{\sigma}_{n+1}^i)^T \mathbf{A}\boldsymbol{\sigma}_{n+1}^i}, \end{aligned} \quad (67)$$

where $\bar{\gamma}_{n+1}^i = \bar{\gamma}_{n+1}^i(\tau_{n+1} - \tau_n)$. The plastic multiplier is obtained from the requirement that the yield function (20) is zero, i.e.

$$\bar{\phi}_{n+1}^i = \bar{\phi}(\boldsymbol{\sigma}_{n+1}^i, \bar{q}(\bar{\zeta}_{n+1}^i(\bar{\gamma}_{n+1}^i))) = \bar{\phi}(\bar{\gamma}_{n+1}^i) = 0. \quad (68)$$

For linear hardening, with hardening modulus $K_h \geq 0$, and

$$\bar{q}_{n+1}^i = -K_h \bar{\zeta}_{n+1}^i, \quad (69)$$

there is a closed-form solution of (68) as

$$\bar{\gamma}_{n+1}^i = \frac{\sigma_y \left(\sigma_y \sqrt{(\boldsymbol{\sigma}_{n+1}^i)^T \mathbf{A}\boldsymbol{\sigma}_{n+1}^i} - \sigma_y - K_h \bar{\zeta}_n^i \right)}{2K_h \sqrt{(\boldsymbol{\sigma}_{n+1}^i)^T \mathbf{A}\boldsymbol{\sigma}_{n+1}^i}} \quad (70)$$

For nonlinear hardening, a local iterative procedure is needed to get $\bar{\gamma}_{n+1}^i$ from (68). Once $\bar{\gamma}_{n+1}^i$ is known, the updates $\bar{\boldsymbol{\epsilon}}_{n+1}^{p,i}$ and $\bar{\zeta}_{n+1}^i$ can be computed with (67).

3.3.1.2. Contribution to the tangent stiffness matrix. Among the vectors in (57), only $\mathbf{f}_{\beta,n+1}^{e,i}$ depends on bulk internal variable, in particular, on plastic strains $\bar{\boldsymbol{\epsilon}}^p$. In order to get components of the stiffness matrix in (57), the derivatives of $\mathbf{f}_{\beta,n+1}^{e,i}$ with respect to plastic strains are needed. They can be obtained by the chain rule as (we will omit superscript i and subscript $n+1$ in eqs. (71), 72 and 74 below):

$$\frac{\partial \bar{\boldsymbol{\epsilon}}^p}{\partial \mathbf{d}^e} = \frac{\partial \bar{\boldsymbol{\epsilon}}^p}{\partial \bar{\boldsymbol{\epsilon}}} \underbrace{\frac{\partial \bar{\boldsymbol{\epsilon}}}{\partial \mathbf{d}^e}}_{\mathbf{B}}, \quad \frac{\partial \bar{\boldsymbol{\epsilon}}^p}{\partial \boldsymbol{\beta}^e} = \frac{\partial \bar{\boldsymbol{\epsilon}}^p}{\partial \boldsymbol{\sigma}} \underbrace{\frac{\partial \boldsymbol{\sigma}}{\partial \boldsymbol{\beta}^e}}_{\mathbf{S}}, \quad \frac{\partial \bar{\boldsymbol{\epsilon}}^p}{\partial \boldsymbol{\alpha}^e} = \frac{\partial \bar{\boldsymbol{\epsilon}}^p}{\partial \bar{\boldsymbol{\epsilon}}} \underbrace{\frac{\partial \bar{\boldsymbol{\epsilon}}}{\partial \boldsymbol{\alpha}^e}}_{\bar{\mathbf{G}}}. \quad (71)$$

The matrices \mathbf{B} and $\bar{\mathbf{G}}$ can be easily constructed by using (9)-(13).

For elastic step, the derivatives of plastic strains are zero because of no change in $\bar{\boldsymbol{\epsilon}}^p$. For plastic step, one has to elaborate on $\frac{\partial \bar{\boldsymbol{\epsilon}}^p}{\partial \bar{\boldsymbol{\epsilon}}}|_{n+1}^i$ and $\frac{\partial \bar{\boldsymbol{\epsilon}}^p}{\partial \boldsymbol{\sigma}}|_{n+1}^i$, which can be obtained from (67) by considering that $\bar{\gamma}_{n+1}^i$ is function of $\boldsymbol{\sigma}_{n+1}^i$ and $\bar{\boldsymbol{\epsilon}}_{n+1}^i$:

$$\frac{\partial \bar{\boldsymbol{\epsilon}}^p}{\partial \bar{\boldsymbol{\epsilon}}} = \frac{\partial \bar{\boldsymbol{\epsilon}}^p}{\partial \bar{\gamma}} \otimes \frac{\partial \bar{\gamma}}{\partial \bar{\boldsymbol{\epsilon}}}, \quad \frac{\partial \bar{\boldsymbol{\epsilon}}^p}{\partial \boldsymbol{\sigma}} = \frac{\partial \bar{\boldsymbol{\epsilon}}^p}{\partial \bar{\gamma}} \otimes \frac{\partial \bar{\gamma}}{\partial \boldsymbol{\sigma}} + \bar{\gamma} 2\mathbf{A}, \quad (72)$$

where

$$\frac{\partial \bar{\boldsymbol{\epsilon}}^p}{\partial \bar{\gamma}} \Big|_{n+1}^i = 2\mathbf{A}\boldsymbol{\sigma}_{n+1}^i. \quad (73)$$

Derivatives $\partial \bar{\gamma} / \partial \bar{\boldsymbol{\epsilon}}|_{n+1}^i$ and $\partial \bar{\gamma} / \partial \boldsymbol{\sigma}|_{n+1}^i$ in (72) can be obtained from the consistency condition $\bar{\gamma} \bar{\phi}|_{n+1}^i = 0$. Because $\bar{\gamma}_{n+1}^i = \bar{\gamma}_{n+1}^i / (\tau_{n+1} - \tau_n) > 0$, the consistency condition holds if

$$\begin{aligned}
0 &= \dot{\bar{\phi}} = \left(\frac{\partial \bar{\phi}}{\partial \boldsymbol{\sigma}} \right)^T \dot{\boldsymbol{\sigma}} + \frac{\partial \bar{\phi}}{\partial \bar{\gamma}} \left(\left(\frac{\partial \bar{\gamma}}{\partial \boldsymbol{\sigma}} \right)^T \dot{\boldsymbol{\sigma}} + \left(\frac{\partial \bar{\gamma}}{\partial \bar{\epsilon}} \right)^T \dot{\bar{\epsilon}} \right) \\
&= \underbrace{\left(\frac{\partial \bar{\phi}}{\partial \boldsymbol{\sigma}} + \frac{\partial \bar{\phi}}{\partial \bar{\gamma}} \frac{\partial \bar{\gamma}}{\partial \boldsymbol{\sigma}} \right)^T}_0 \underbrace{\dot{\boldsymbol{\sigma}}}_{\neq 0} + \underbrace{\frac{\partial \bar{\phi}}{\partial \bar{\gamma}} \left(\frac{\partial \bar{\gamma}}{\partial \bar{\epsilon}} \right)^T}_{\neq 0} \underbrace{\dot{\bar{\epsilon}}}_{\neq 0}. \quad (74)
\end{aligned}$$

Since $\dot{\boldsymbol{\sigma}}_{n+1}^i \neq 0$ and $\dot{\bar{\epsilon}}_{n+1}^i \neq 0$, the consistency condition leads to

$$\frac{\partial \bar{\gamma}}{\partial \bar{\epsilon}} \Big|_{n+1}^i = \mathbf{0}, \quad \frac{\partial \bar{\gamma}}{\partial \boldsymbol{\sigma}} \Big|_{n+1}^i = - \left(\frac{\partial \bar{\phi}}{\partial \bar{\gamma}} \right)^{-1} \frac{\partial \bar{\phi}}{\partial \boldsymbol{\sigma}} \Big|_{n+1}^i. \quad (75)$$

By using (75) and (73) in (72), the two searched expressions are:

$$\begin{aligned}
\frac{\partial \bar{\epsilon}^p}{\partial \bar{\epsilon}} \Big|_{n+1}^i &= \mathbf{0}, \quad \frac{\partial \bar{\epsilon}^p}{\partial \boldsymbol{\sigma}} \Big|_{n+1}^i \\
&= \left[-2\mathbf{A}\boldsymbol{\sigma} \otimes \left(\frac{\partial \bar{\phi}}{\partial \bar{\gamma}} \right)^{-1} \frac{\partial \bar{\phi}}{\partial \boldsymbol{\sigma}} \right]_{n+1}^i + \bar{\gamma}_{n+1}^i 2\mathbf{A}, \quad (76)
\end{aligned}$$

which suggests that the three required derivatives in (71) are:

$$\frac{\partial \bar{\epsilon}^p}{\partial \mathbf{d}^e} \Big|_{n+1}^i = \mathbf{0}, \quad \frac{\partial \bar{\epsilon}^p}{\partial \boldsymbol{\beta}^e} \Big|_{n+1}^i = \underbrace{\frac{\partial \bar{\epsilon}^p}{\partial \boldsymbol{\sigma}}}_{(76)} \mathbf{S}_{n+1}^i, \quad \frac{\partial \bar{\epsilon}^p}{\partial \boldsymbol{\alpha}^e} \Big|_{n+1}^i = \mathbf{0}. \quad (77)$$

For linear hardening (69), $\frac{\partial \bar{\phi}}{\partial \boldsymbol{\sigma}} \Big|_{n+1}^i = 2\mathbf{A}\boldsymbol{\sigma}_{n+1}^i$ and $\frac{\partial \bar{\phi}}{\partial \bar{\gamma}} \Big|_{n+1}^i = -\frac{4K_0 \boldsymbol{\sigma}_{n+1}^{i,T} \mathbf{A} \boldsymbol{\sigma}_{n+1}^i}{\sigma_y^2}$. With (77), we can compute the terms of the tangent stiffness matrix related to the derivatives of plastic strains.

3.3.2. Discontinuity

In this section, we present computation of iterative values of displacement-like softening variable $\bar{\zeta}_{n+1}^{g,i}$ and tractions $\mathbf{t}_{n+1}^{g,i}$ at discontinuity integration point g . We first read plastic variables from the last converged configuration at τ_n : $\bar{\mathbf{u}}_n^g = [\bar{\mathbf{u}}_{n,n}^g, \bar{\mathbf{u}}_{m,n}^g]^T$ and $\bar{\zeta}_n^g$. Here, $\bar{\mathbf{u}}_{n,n}^g = \alpha_{1,n} + \zeta_\Gamma^g \alpha_{2,n}$ and $\bar{\mathbf{u}}_{m,n}^g = \alpha_{3,n} + \zeta_\Gamma^g \alpha_{4,n}$ are normal and tangential components of displacement jumps, respectively. We also compute current values of displacement jumps

$$\begin{aligned}
\bar{\mathbf{u}}_{n+1}^{g,i} &= [\bar{\mathbf{u}}_{n,n+1}^{g,i}, \bar{\mathbf{u}}_{m,n+1}^{g,i}]^T \\
&= [\alpha_{1,n+1}^i + \zeta_\Gamma^g \alpha_{2,n+1}^i, \alpha_{3,n+1}^i + \zeta_\Gamma^g \alpha_{4,n+1}^i]^T, \quad (78)
\end{aligned}$$

and check for change of discontinuity parameters

$$\|\bar{\mathbf{u}}_{n+1}^{g,i} - \bar{\mathbf{u}}_n^g\| \stackrel{?}{\leq} tol \quad \text{or} \quad \|\boldsymbol{\alpha}_{n+1}^{g,i} - \boldsymbol{\alpha}_n^g\| \stackrel{?}{\leq} tol, \quad (79)$$

which represents change of plastic deformations at discontinuity.

3.3.2.1. Trial-correction procedure. We deal with rigid plasticity with softening. In order to be able to use standard trial-correction procedure for plasticity, we treat (45) as constitutive equation for \mathbf{t} . In the trial phase, we use (45) in order to obtain trial values of tractions in the two discontinuity integration points

$$\mathbf{f}_{z,n+1}^{\Omega^e, e, i} + \mathbf{f}_{z,n+1}^{\Gamma^e, e, i} \left(\mathbf{t}_{n+1}^{1, trial, i}, \mathbf{t}_{n+1}^{2, trial, i} \right) = \mathbf{0} \Rightarrow \mathbf{t}_{n+1}^{1, trial, i}, \mathbf{t}_{n+1}^{2, trial, i}. \quad (80)$$

The resulting equations (80) for the components of $\mathbf{t}_{n+1}^{1, trial, i}$ and $\mathbf{t}_{n+1}^{2, trial, i}$ are

$$\mathbf{t}^e \int_{\Omega^e} \begin{bmatrix} \bar{\mathbf{G}}_1^T \boldsymbol{\sigma}_{n+1}^i \\ \bar{\mathbf{G}}_2^T \boldsymbol{\sigma}_{n+1}^i \\ \bar{\mathbf{G}}_3^T \boldsymbol{\sigma}_{n+1}^i \\ \bar{\mathbf{G}}_4^T \boldsymbol{\sigma}_{n+1}^i \end{bmatrix} d\Omega + \sum_{g=1}^2 \frac{w_g l_\Gamma t^e}{2} \begin{bmatrix} \mathbf{t}_{n,n+1}^{g, trial, i} \\ \zeta_\Gamma^g \\ \mathbf{t}_{m,n+1}^{g, trial, i} \\ \zeta_\Gamma^g \end{bmatrix} = \mathbf{0}, \quad (81)$$

where $w_1 = w_2 = 1$ are integration weights and $\zeta_\Gamma^g = \frac{\zeta_e l_\Gamma}{2}$ is integration point location ($\zeta_1 = -\frac{\sqrt{3}}{3}, \zeta_2 = \frac{\sqrt{3}}{3}$). Next, we evaluate the failure function with the trial values $\mathbf{t}_{n+1}^{g, trial, i}$ and $\bar{\zeta}_{n+1}^{g, trial, i} = \bar{\zeta}_n^g$ and check its admissibility

$$\bar{\phi}_{n+1}^{g, trial, i} = \bar{\phi} \left(\mathbf{t}_{n+1}^{g, trial, i}, \bar{q} \left(\bar{\zeta}_n^g \right) \right) \stackrel{?}{\leq} 0. \quad (82)$$

We have now several possible cases at integration point regarding criteria (79) and (82):

$$(79) \text{ is true and } \begin{cases} (82) \text{ is true} \Rightarrow \text{case (a) on Fig.5} \\ (82) \text{ is false} \Rightarrow \text{case (b) on Fig.5} \end{cases} \quad (83)$$

(79) is false \Rightarrow case (c) on Fig.5.

For case (a) on Figure 5, pseudo-time increment for current iteration is elastic. The value of softening plasticity variable remains unchanged and tractions equal to trial ones, i.e. $\bar{\zeta}_{n+1}^{g,i} = \bar{\zeta}_n^g$ and $\mathbf{t}_{n+1}^{g,i} = \mathbf{t}_{n+1}^{g, trial, i}$. For case (b) on Figure 5, the softening plasticity variable remains unchanged and tractions are computed by enforcing admissibility of the failure function, i.e.

$$\bar{\zeta}_{n+1}^{g,i} = \bar{\zeta}_n^g \quad \text{and} \quad \bar{\phi}_{n+1}^{g,i} = \bar{\phi} \left(\mathbf{t}_{n+1}^{g,i}, \bar{q} \left(\bar{\zeta}_n^g \right) \right) = 0 \Rightarrow \mathbf{t}_{n+1}^{g,i}. \quad (84)$$

For case (c) on Figure 5, new value of softening plasticity variable is computed by exploiting double meaning of $\bar{\mathbf{u}}$. Namely, from the kinematic point of view, $\bar{\mathbf{u}}$ represent displacement jumps and from the constitutive relations point of view, $\bar{\mathbf{u}}$ represent plastic deformations. By using the backward Euler scheme for a discrete form of equation (26), one has

$$\bar{\mathbf{u}}_{n+1}^{g,i} = \bar{\mathbf{u}}_n^g + \bar{\gamma}_{n+1}^{g,i} \frac{\partial \bar{\phi}}{\partial \mathbf{t}} \Big|_{n+1}^{g,i}. \quad (85)$$

Of course, values from (78) should equal those from (85). By exploiting this fact, the plastic multiplier can be computed as

$$\bar{\gamma}_{n+1}^{g,i} = \left(\bar{\mathbf{u}}_{n+1}^{g,i, (78)} - \bar{\mathbf{u}}_n^g \right)^T \left(\frac{\partial \bar{\phi}}{\partial \mathbf{t}} \right)^{-1} \Big|_{n+1}^{g,i} \geq 0. \quad (86)$$

Having determined $\bar{\gamma}_{n+1}^{g,i}$, we can proceed by computing new value of strain-like softening variable by the backward Euler integration scheme

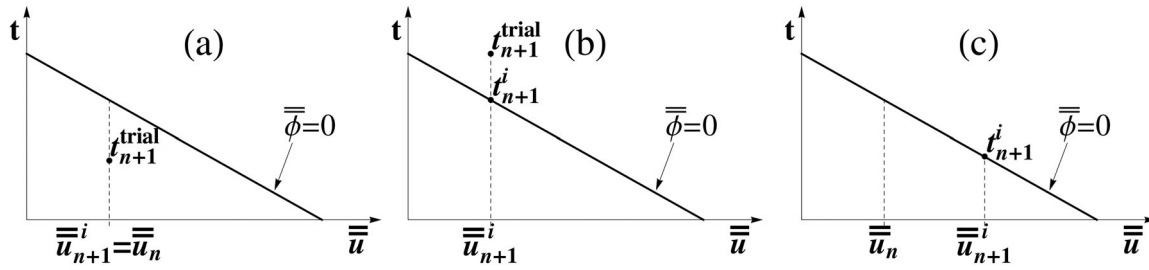


Figure 5. The discontinuity integration point: (a) the elastic step, (b) the plastic step with $\bar{u}_{n+1}^i = \bar{u}_n$, and (c) the plastic step with $\bar{u}_{n+1}^i \neq \bar{u}_n$.

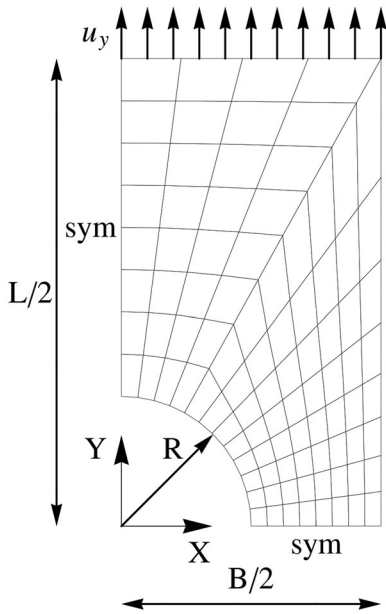


Figure 6. Strip with a hole: geometry and boundary conditions. The mesh consists of 96 elements and 117 nodes.

$$\bar{\zeta}_{n+1}^{g,i} = \bar{\zeta}_n^g + \bar{\gamma}_{n+1}^{g,i} \frac{\partial \bar{\phi}}{\partial \bar{q}} \Big|_{n+1}^{g,i} \quad (87)$$

Current values of tractions at an integration point are determined by demanding admissible (i.e. zero) value of the failure function (24),

$$\bar{\phi}_{n+1}^{g,i} = \bar{\phi} \left(\bar{t}_{n+1}^{g,i}, \bar{q} \left(\bar{\zeta}_{n+1}^{g,i} \right) \right) = 0 \Rightarrow \bar{t}_{n+1}^{g,i} \quad (88)$$

3.3.2.2. Contribution to the tangent stiffness matrix. In order to compute $\left(\frac{\partial \bar{t}}{\partial \bar{\alpha}} \right)_{n+1}^{e,i}$, see (58), one needs to derive

$$\frac{\partial \bar{t}}{\partial \bar{\alpha}} \Big|_{n+1}^{g,i} = \frac{\partial \bar{t}}{\partial \bar{\mathbf{u}}} \frac{\partial \bar{\mathbf{u}}}{\partial \bar{\alpha}} \Big|_{n+1}^{g,i} = \mathbf{K}_{\alpha\alpha, n+1}^{e,i} \quad (89)$$

For case (a) on Figure 5, we choose $\mathbf{K}_{\alpha\alpha, n+1}^{e,i} = 0$, and the conditioning of $\mathbf{K}_{hh, n+1}^{e,i}$ has to be checked. If discontinuity divides element into two parts with 2 nodes, the conditioning of $\mathbf{K}_{hh, n+1}^{e,i}$ is good. Otherwise, if there is a part with a single node, $\mathbf{K}_{hh, n+1}^{e,i}$ is badly conditioned and the procedure from Section 3.2.4 applies.

For cases (b) and (c) on Figure 5, the term $\frac{\partial \bar{\mathbf{u}}}{\partial \bar{\alpha}} \Big|_{n+1}^{g,i}$ can be obtained from (78), and $\frac{\partial \bar{t}}{\partial \bar{\mathbf{u}}} \Big|_{n+1}^{g,i}$ is obtained by the chain rule as:

$$\frac{\partial \bar{t}}{\partial \bar{\mathbf{u}}} \Big|_{n+1}^{g,i} = \frac{\partial \bar{t}}{\partial \bar{\gamma}} \otimes \frac{\partial \bar{\gamma}}{\partial \bar{\mathbf{u}}} \Big|_{n+1}^{g,i}, \quad \frac{\partial \bar{\gamma}}{\partial \bar{\mathbf{u}}} \Big|_{n+1}^{g,i} \stackrel{(86)}{=} \left(\frac{\partial \bar{\phi}}{\partial \bar{\mathbf{t}}} \right) \Big|_{n+1}^{g,i} \quad (90)$$

where $\frac{\partial \bar{t}}{\partial \bar{\gamma}} \Big|_{n+1}^{g,i}$ in (90) follows from the consistency condition $\frac{\partial \bar{\phi}}{\partial \bar{\gamma}} \Big|_{n+1}^{g,i} = 0$. Because $\bar{\gamma}_{n+1}^{g,i} = \bar{\gamma}_{n+1}^{g,i} (\tau_{n+1} - \tau_n) \neq 0$, one considers

$$0 = \frac{\partial \bar{\phi}}{\partial \bar{\gamma}} \Big|_{n+1}^{g,i} = \underbrace{\left(\frac{\partial \bar{\phi}}{\partial \bar{\mathbf{t}}} + \frac{\partial \bar{\phi}}{\partial \bar{\gamma}} \right)^T}_{=0} \bar{\mathbf{t}} \Big|_{n+1}^{g,i}, \quad (91)$$

which leads to

$$\frac{\partial \bar{t}}{\partial \bar{\gamma}} \Big|_{n+1}^{g,i} = - \left(\frac{\partial \bar{\phi}}{\partial \bar{\gamma}} \right) \left(\frac{\partial \bar{\phi}}{\partial \bar{\mathbf{t}}} \right)^{-1} \Big|_{n+1}^{g,i} \quad (92)$$

By using (92) and (90)₂ in (90)₁, one finally gets

$$\frac{\partial \bar{t}}{\partial \bar{\mathbf{u}}} \Big|_{n+1}^{g,i} = - \left(\frac{\partial \bar{\phi}}{\partial \bar{\gamma}} \right) \left(\frac{\partial \bar{\phi}}{\partial \bar{\mathbf{t}}} \right)^{-1} \otimes \left(\frac{\partial \bar{\phi}}{\partial \bar{\mathbf{t}}} \right)^{-1} \Big|_{n+1}^{g,i}, \quad (93)$$

which concludes the derivation of $\mathbf{K}_{\alpha\alpha, n+1}^{e,i}$ in (89).

4. Numerical examples

The finite element code was developed by using capabilities of automatic differentiation of Mathematica's add-on AceGen [40]. The code was included into the finite element code AceFem [41].

4.1. Elasto-plastic analysis of strip with hole

With this example, we test the proposed stress-driven algorithm for elasto-plasticity for the Hellinger-Reissner formulation. Figure 6 shows mesh and boundary conditions (one quadrant is modeled with conditions considering symmetry) for the problem with geometry: $L = 36$ mm, $B = 20$ mm, thickness $t = 1$ mm and $R = 5$ mm. The material data is: elastic modulus $E = 70$ kN/mm², Poisson's ratio $\nu = 0$, yield stress $\sigma_y = 0.243$ kN/mm² and isotropic hardening modulus $K_h = 0.2$ kN/mm². The strip is loaded by prescribed displacements. In Figure 7, we show the reaction force versus the prescribed displacement curve and compare it with results of algorithms from Fuschi et al. [42] and Dujc and Brank [43]. The results are practically identical. In [42], a standard, plane stress, returning-mapping for von Mises elasto-plasticity was used. In [43], an Ilyushin-Shapiro, stress resultant, elasto-plasticity was used. In both [42] and [43],

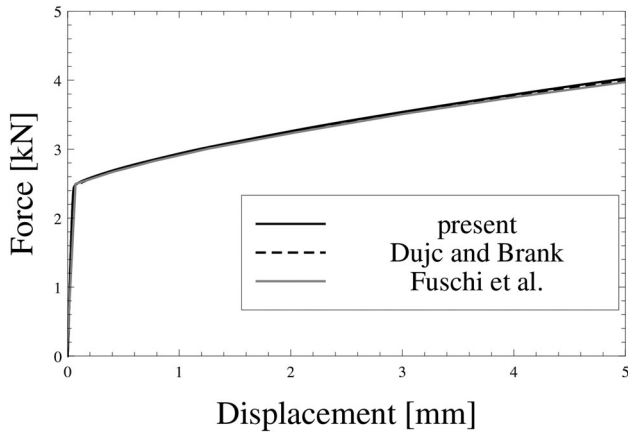


Figure 7. Strip with a hole: edge force versus prescribed displacement.

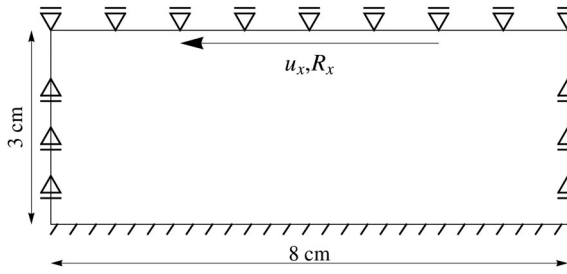


Figure 8. Shear test: geometry and the boundary conditions.

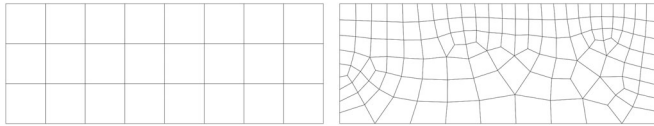


Figure 9. Shear test: meshes. The structured mesh consists of 24 elements and 36 nodes and the unstructured one of 130 elements and 156 nodes.

the algorithm was strain-driven, in contrast to the present one, which is stress-driven.

4.2. Shear test

We consider the strip on Figure 8 with the following data: Young's modulus $E = 20690 \text{ kN/cm}^2$, Poisson's ratio $\nu = 0.29$, failure shear strength $\tau_u = 45 \text{ kN/cm}^2$, softening modulus $K_s = -200 \text{ kN/cm}^3$, and thickness $t = 1 \text{ cm}$.

The softening at discontinuity is governed by the following failure and softening functions

$$\bar{\phi}(t, \bar{q}) = |t_m| - (\tau_u - \bar{q}), \quad (94)$$

$$\bar{q} = \min[\tau_u, -K_s \bar{\xi}]. \quad (95)$$

We consider only mode II sliding at the discontinuity, i.e. $\alpha_1 = \alpha_2 = 0$. The left-edge mid-point is the starting point for the tracking algorithm. Figure 9 presents the two used finite element meshes, and Figure 10 shows perfect agreement of our force versus imposed displacement curves with those from Mosler [44] for elastic bulk. Results for elasto-plastic bulk, with yield stress $\sigma_y = 60 \text{ kN/cm}^2$ and hardening modulus $K_h = E/10$, are also presented in Figure 10, with three phases of response: elastic, plastic hardening and

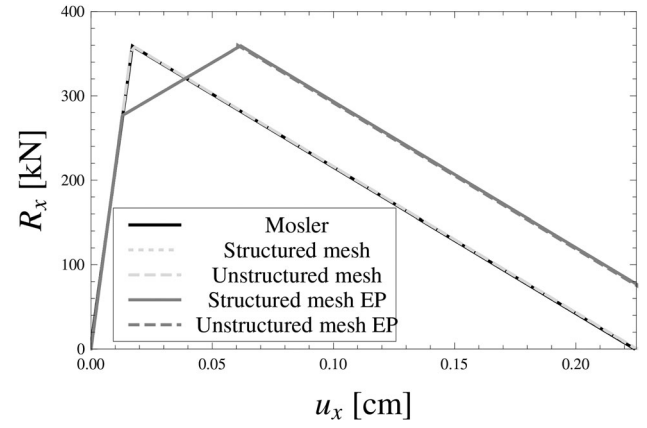


Figure 10. The force versus the displacement curves for the shear test.

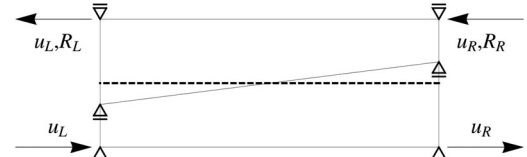


Figure 11. Test for the stabilization parameter: geometry and mesh.

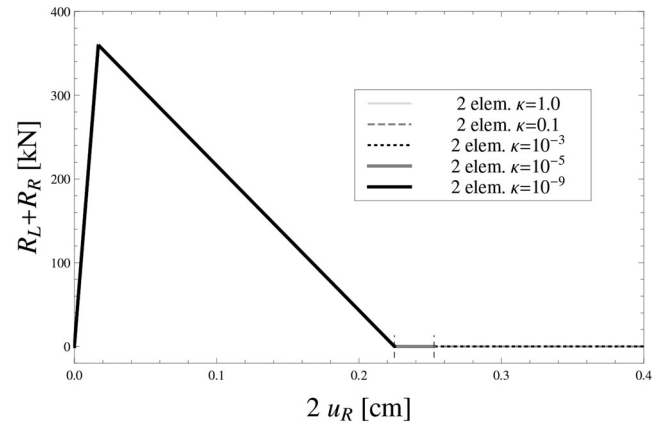


Figure 12. Force versus displacement curves for different values of κ .

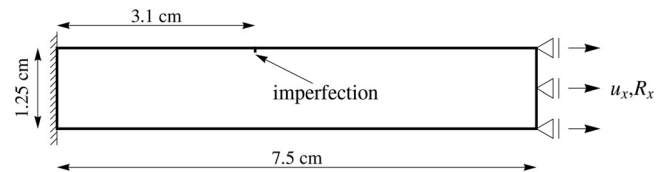


Figure 13. The geometry of metal strip.

localized plastic softening. Both coarse structured and finer unstructured mesh produce identical results.

4.3. Test for stabilization parameter κ

With this test we check for the influence of the stabilization parameter κ on the results. We consider a rectangular ($8 \text{ cm} \times 3 \text{ cm}$) strip with the following data: Young's modulus $E = 20690 \text{ kN/cm}^2$, Poisson's ratio $\nu = 0.29$, failure shear strength $\tau_u = 45 \text{ kN/cm}^2$, softening modulus $K_s =$

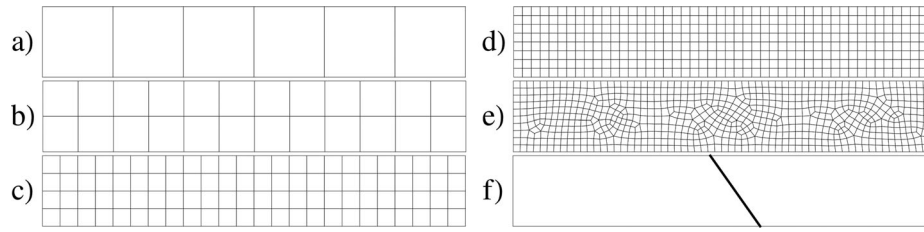


Figure 14. Metal strip: a) structured mesh with 6 elements and 14 nodes, b) structured mesh with 24 elements and 39 nodes, c) structured mesh with 96 elements and 125 nodes, d) structured mesh with 384 elements and 441 nodes, e) unstructured mesh with 720 elements and 794 nodes, and f) slip lines for the meshes.

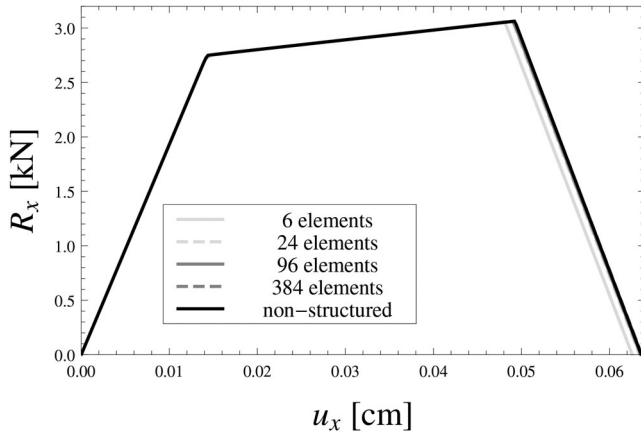


Figure 15. The force versus the displacement curves for the metal strip.

-200kN/cm^3 , and thickness $t = 1\text{ cm}$. Only mode II sliding at discontinuity is adopted, i.e. $\alpha_1 = \alpha_2 = 0$, with the softening governed by 94 and 95. Used mesh, boundary conditions, and a predefined cohesive line are shown in Figure 11. The latter crosses both elements in such a way that it separates one node at each element. The loading is imposed by prescribed displacements u_L and u_R . Before the slip outset $u_L = u_R$ and after the slip outset $u_L = 0.999u_R$ in order to activate the linear variation of the tangential slip along the cohesive line. Figure 12 shows force-displacement curves for different values of κ . The stabilization procedure with κ is activated if the traction at the discontinuity integration point drops to zero. If the value of κ is too small, the convergence is lost. For $\kappa = 10^{-3}$, the analysis becomes stable. In general, an optimal (i.e. minimal possible) value for κ depends on matrix $\mathbf{K}_{\alpha\alpha}^e$.

4.4. Elasto-plastic strip

The geometry and the boundary conditions of a metal strip, which is loaded by imposed displacements on its right edge, are presented in Figure 13. The data are: Young's modulus $E = 21000\text{kN/cm}^2$, Poisson's ratio $\nu = 0.29$, yield stress $\sigma_y = 40\text{kN/cm}^2$, hardening modulus $K_h = 1000\text{kN/cm}^2$, failure shear strength $\tau_u = 21\text{kN/cm}^2$, softening modulus $K_s = -400\text{kN/cm}^3$, and thickness $t = 0.055\text{cm}$. The softening response is governed by mode II fracture ($\alpha_1 = \alpha_2 = 0$), with (94) and (95). The strip has a small imperfection (see Figure 13), which is used as a starting point for the tracking algorithm. Figure 14 indicates that the edge reaction versus the imposed displacement is practically the same for the meshes shown in Figure 15.

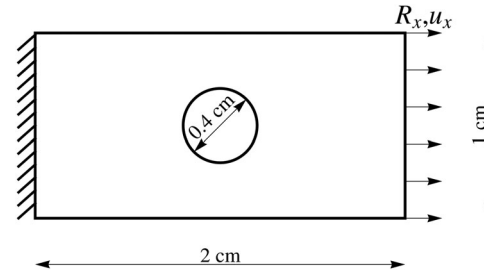


Figure 16. The geometry of the steel strip with a hole.

The computed angles Θ_{cr} are: 35.22° for mesh a), 35.26° for meshes b), c) and e), and 35.27° for mesh d). This is in nice agreement with $\Theta_{cr} = 35.26^\circ$ reported in [39].

4.5. Strip with a hole

The problem on Figure 16 was investigated by Mosler [44] for the following data: Young's modulus $E = 20690\text{kN/cm}^2$, Poisson's ratio $\nu = 0.29$, failure shear strength $\tau_u = 45\text{kN/cm}^2$, softening modulus $K_s = -4000\text{kN/cm}^3$, and thickness $t = 0.1\text{ cm}$. The softening is governed by (94) and (95). Figure 17 shows finite element meshes. Two slip lines appear: one above and one below the hole. Our formulation can track one slip line within one domain, thus we divided each mesh into two domains corresponding to the lower and upper half of the strip.

In Figure 18, we plot force versus displacement curves and the corresponding slip lines for elastic bulk. The curves are compared with the ones from Mosler [44], with the former showing slightly higher limit loads. The mesh has an effect on results, which can be associated with large stress gradients around the hole. Analysis with elasto-plastic bulk was performed for yield stress $\sigma_y = 80\text{kN/cm}^2$ and hardening modulus $K_h = E/10$. In Figure 19, we show the load-displacement curves and the corresponding slip lines. All curves are similar up to $u_x \approx 0.009\text{cm}$, and after that we have slightly different responses. We plot in Figure 20 the energy/work versus the imposed displacement for the super-fine mesh. The elastic energy at the pseudo-time $\tau_{\bar{n}}$ (associated with the \bar{n}^{th} incremental step) equals (see (27))

$$W_e(\tau_{\bar{n}}) = \sum_{e=1}^{N_{el}} \Pi^{int,e} \Big|_{\tau=\tau_{\bar{n}}}, \quad (96)$$

the plastic work related to the hardening at the pseudo-time $\tau_{\bar{n}}$ is computed as

$$W_h(\tau_{\bar{n}}) = \sum_{l=1}^{\bar{n}} \sum_{e=1}^{N_{el}} t^e \int_{\Omega^e} (\bar{\xi}_l - \bar{\xi}_{l-1}) (\sigma_y + K_h \bar{\xi}_l) d\Omega, \quad (97)$$

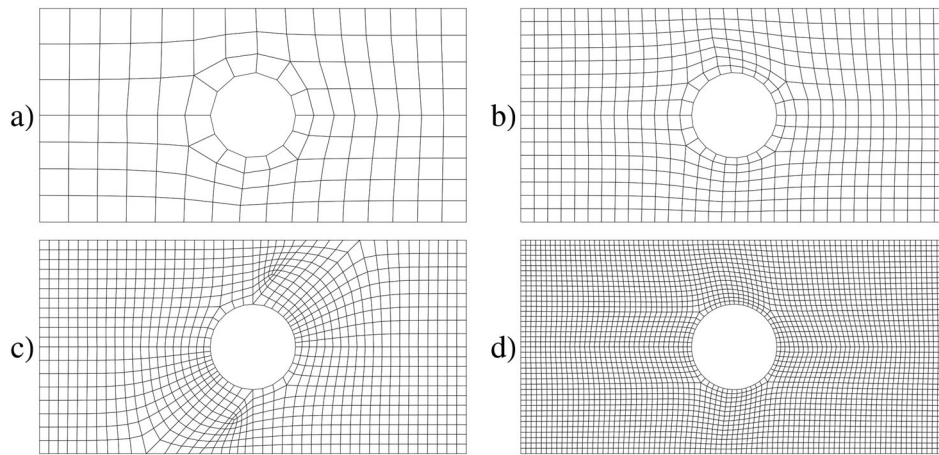


Figure 17. Meshes: a) coarse mesh with 129 elements and 159 nodes, b) fine mesh with 502 elements and 561 nodes, c) aligned mesh with 962 elements and 1042 nodes, and d) super-fine mesh with 3241 elements and 3392 nodes.

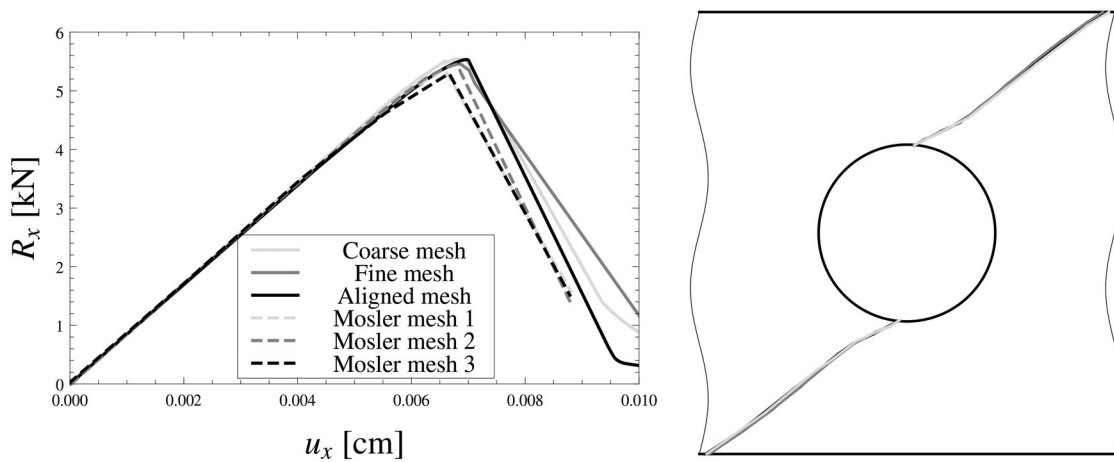


Figure 18. Force versus the displacement curves (left) and the corresponding slip lines (right).

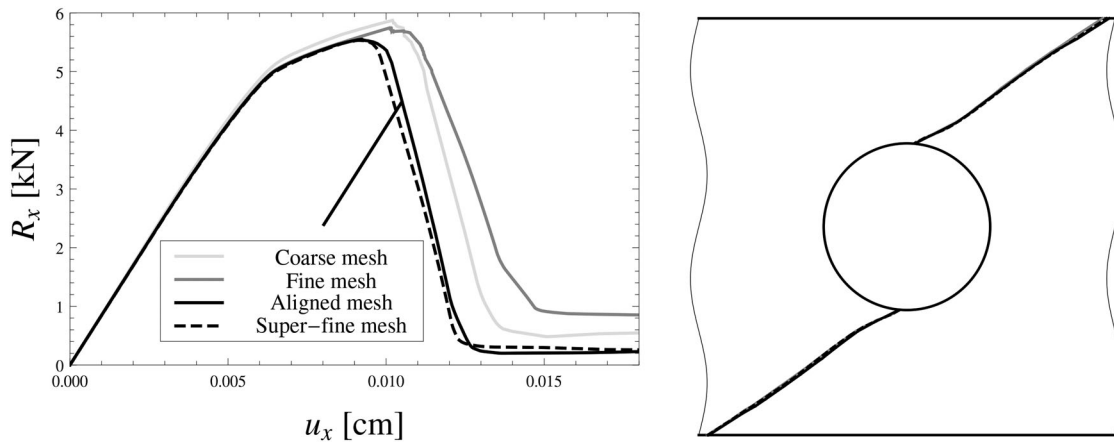


Figure 19. Force versus the displacement curves for the elasto-plastic bulk (left) and the corresponding slip lines (right).

and the plastic work related to the localized softening at pseudo-time $\tau_{\bar{n}}$ is

$$W_s(\tau_{\bar{n}}) = \sum_{l=1}^{\bar{n}} \sum_{e=1}^{N_{el}} t^e \int_{\Gamma^e} (\bar{\mathbf{u}}_l - \bar{\mathbf{u}}_{l-1}) \cdot \mathbf{t}_l d\Gamma. \quad (98)$$

Figure 20 shows that W_s increases rapidly after both cracks are completely formed. Once the cohesion at the cracks is lost, W_s remains constant. W_h slightly increases even after

the complete decohesion takes place at both cracks. This is because the cracks are not straight lines, see Figure 19, and only mode II fracture is assumed. In Figure 21, we plot W_s for different meshes. The point when a curve starts to rise sharply is slightly different for each mesh. These points correspond to the limit-loads. The total softening plastic work at collapse is practically the same for all meshes.

4.6. Computational times and efficiency

The Table 1 summarizes the computational times and the efficiency of the present formulation observed with the numerical examples presented in Sections 4.1, 4.2, 4.4 and 4.5. The load-application algorithm was relatively simple with a prescribed minimal and a maximal value of the load-

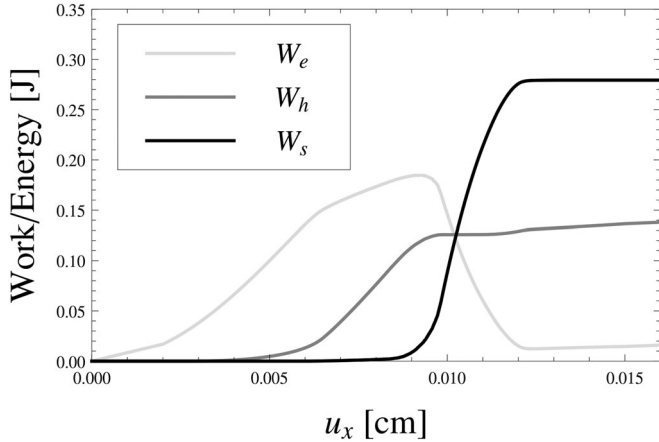


Figure 20. Energy/work versus the imposed displacement curves for super-fine mesh.

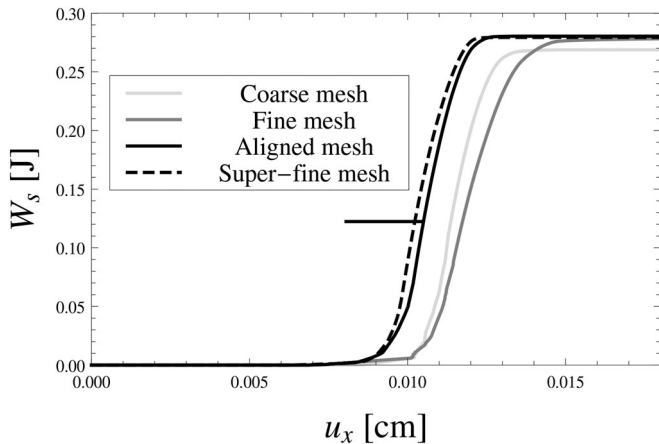


Figure 21. Softening plastic work versus imposed displacement.

increment-size which was adjusted based on the number of iterations in the previous steps. No particular measure to reduce the computational time was used. The simulation times reported in Table 1 were observed on a personal laptop with the 2.5 GHz Intel Core i7 processor and the 16 GB 1600 MHz DDR3 memory.

The present finite element formulation was relatively robust for the tested cases. The value of the average number of iterations per step lies between 4 and 7 and the efficiencies of the simulations, computed as the ratio between the number of step-backs and the total number of steps, were in most cases 100% or very close to 100%. The only exception to this behavior was the case presented in Section 4.1. Note that in this case the softening of the material was not considered and that a very large portion of the geometry was deforming in the plastic regime.

5. Conclusions

Failure analysis of 2d J_2 solids has been addressed in this work, and the embedded-discontinuity finite element method has been used to that end. We have presented a derivation (that includes many details) of the embedded-strong-discontinuity, stress-hybrid, quadrilateral finite element (based on the Hellinger-Reissner functional), with the Pian-Sumihara stress interpolations. The formulation uses J_2 elasto-plasticity for the bulk of the element, and softening plasticity for description of localized cohesion in the interface that extends across the element and represents crack or slip line.

It is worth noting that mixed or hybrid methods (in general) do not apply for triangular elements, and for this reason, the popular embedded discontinuity triangular formulations cannot be extended by using the concept presented herein.

The motivation behind the presented work is the fact that the Pian-Sumihara element delivers the best stress convergence among the mixed quadrilateral formulations, and we consider this important for the embedded-discontinuity formulation. Namely, when and how to embed the

Table 1. The summary of simulations' efficiencies including the number of equations, the total number of steps, the total number of step-backs, the step efficiency, the total number of iterations, the average number of iterations per step, the total time, and the average time per iteration for the examples presented in Sections 4.1, 4.2, 4.4 and 4.5. In the Example column the letter E denotes the elastic response of the bulk while P represents the elasto-plastic response.

Example	Mesh	Equations	Steps	Step-backs	Efficiency (%)	Iter.	Iter./step	Time (s)	Time/iter. (s)
4.1 - P		211	855	371	69.7	13126	10.71	2231.33	0.1700
4.2 - E	struct.	32	91	0	100.0	439	4.82	169.60	0.3863
4.2 - E	unstr.	227	93	3	96.9	586	6.10	514.01	0.8772
4.2 - P	struct.	32	377	0	100.0	2038	5.41	425.16	0.2086
4.2 - P	unstr.	227	752	0	100.0	3867	5.14	2973.85	0.7690
4.4 - P	6 el.	22	1322	23	98.3	7539	5.61	27.77	0.0037
4.4 - P	24 el.	69	1318	2	99.8	7843	5.94	29.14	0.0037
4.4 - P	96 el.	235	1317	0	100.0	7989	6.07	36.69	0.0046
4.4 - P	384 el.	855	1317	0	100.0	8100	6.15	153.52	0.0190
4.4 - P	unstr.	1555	1317	0	100.0	8115	6.16	503.55	0.0621
4.5 - E	coarse	292	792	0	100.0	3610	4.56	201.88	0.0559
4.5 - E	fine	1071	416	0	100.0	1730	4.16	99.66	0.0576
4.5 - E	aligned	2024	692	0	100.0	3091	4.47	114.27	0.0370
4.5 - P	coarse	292	4560	0	100.0	26591	5.83	401.99	0.0151
4.5 - P	fine	1071	1850	0	100.0	11784	6.37	353.50	0.0300
4.5 - P	su.-fine	6659	1303	0	100.0	9441	7.25	744.00	0.0788
4.5 - P	aligned	2024	1850	0	100.0	11950	6.46	362.82	0.0304

discontinuity depends largely on the element stress state, which should be therefore computed as accurate as possible. The derived element takes the best available quadrilateral and extends it for fracture modeling by using the concepts of the embedded-strong-discontinuity finite element method. However, it is worth noting that once the discontinuity is embedded, the accuracy of the element with a crack does not depend too much on how accurate the computation of the element stresses is, but rather on the issues related to the fracture, like ability to avoid the stress-locking, efficiency of the applied traction-separation cohesive law at the discontinuity, ability to describe kinematics of the crack correctly, and effectiveness of the implementation of the fracture aspects of the formulation. Of course, an efficient crack tracking algorithm is also important for a robust fracture analysis.

The theory, the implementation aspects and the computational procedure of the presented formulation are given in detail. Because of the inelastic Hellinger-Reissner formulation, a development of the stress-driven update algorithm was necessary for J_2 elasto-plasticity that was applied for the bulk of the element. The algorithm that was derived works nicely for non-zero isotropic hardening and allows for a simple update at bulk's integration point. Basically, the hardening parameter is updated in a way that the computed stresses become admissible when the step is plastic. The derived algorithm can also be applied for standard elastoplastic formulations (i.e. those not taking into account fracture modeling) with hardening.

Another nonstandard procedure was adopted for the treatment of localized softening plasticity. In order to implement the plasticity with softening in the framework of the standard trial-correction technique, local (i.e. element) equilibrium equations were used to compute the trial values of the tractions at the discontinuity, which deviates the present implementation of the embedded-discontinuity from more standard ones.

Funding

The financial support of Slovenian Research Agency (project J2-1722) is gratefully acknowledged.

References

- [1] T. Rabczuk, Computational methods for fracture in brittle and quasi-brittle solids: State-of-the-art review and future perspectives, *ISRN Appl. Math.*, vol. 2013, pp. 1–38, 2013. DOI: [10.1155/2013/849231](https://doi.org/10.1155/2013/849231).
- [2] J. C. Simo, J. Oliver, and F. Armero, An analysis of strong discontinuities induced by strain-softening in rate-independent inelastic solids, *Comput. Mech.*, vol. 12, no. 5, pp. 277–296, 1993. DOI: [10.1007/BF00372173](https://doi.org/10.1007/BF00372173).
- [3] E. Dvorkin, A. M. Cuitiño, and G. Gioia, Finite elements with displacement interpolated embedded localization lines insensitive to mesh size and distortions, *Int. J. Numer. Meth. Engng.*, vol. 30, no. 3, pp. 541–564, 1990. DOI: [10.1002/nme.1620300311](https://doi.org/10.1002/nme.1620300311).
- [4] D. Brancherie, and A. Ibrahimbegovic, Novel anisotropic continuum-discrete damage model capable of representing localized failure of massive structures. Part I: theoretical formulation and numerical implementation, *Eng. Comput.*, vol. 26, no. 1/2, pp. 100–127, 2009. DOI: [10.1108/02644400910924825](https://doi.org/10.1108/02644400910924825).
- [5] D. Dias-da-Costa, J. Alfaiate, L. J. Sluys, and E. Júlio, Towards a generalization of a discrete strong discontinuity approach, *Comput. Methods Appl. Mech. Engrg.*, vol. 198, pp. 3680–3681, 2009.
- [6] M. Jirasek, Comparative study on finite elements with embedded discontinuities, *Comput. Methods Appl. Mech. Engrg.*, vol. 188, pp. 307–330, 2000.
- [7] Y. Zhang, R. Lackner, M. Zeiml, and H. A. Mang, Strong discontinuity embedded approach with standard SOS formulation: Element formulation, energy-based crack-tracking strategy, and validations, *Comput. Methods Appl. Mech. Engrg.*, vol. 287, pp. 335–366, 2015. DOI: [10.1016/j.cma.2015.02.001](https://doi.org/10.1016/j.cma.2015.02.001).
- [8] J. Oliver, A. E. Huespe, S. Blanco, and D. L. Linero, Stability and robustness issues in numerical modeling of material failure with the strong discontinuity approach, *Comput. Methods Appl. Mech. Engrg.*, vol. 195, no. 52, pp. 7093–7114, 2006. DOI: [10.1016/j.cma.2005.04.018](https://doi.org/10.1016/j.cma.2005.04.018).
- [9] J. Oliver, A. E. Huespe, and I. F. Dias, Strain localization, strong discontinuities and material fracture: matches and mismatches, *Comput. Methods Appl. Mech. Engrg.*, vol. 241–244, pp. 323–336, 2012. DOI: [10.1016/j.cma.2012.06.004](https://doi.org/10.1016/j.cma.2012.06.004).
- [10] J. Alfaiate, A. Simone, and L. J. Sluys, Non-homogenous displacement jumps in strong embedded discontinuities, *Int. J. Solids Struct.*, vol. 40, no. 21, pp. 5799–5817, 2003. DOI: [10.1016/S0020-7683\(03\)00372-X](https://doi.org/10.1016/S0020-7683(03)00372-X).
- [11] F. Armero, and D. Ehrlich, Finite element methods for the multi-scale modeling of softening lines in plates at failure, *Comput. Methods Appl. Mech. Engrg.*, vol. 195, no. 13–16, pp. 1283–1324, 2006a. DOI: [10.1016/j.cma.2005.05.040](https://doi.org/10.1016/j.cma.2005.05.040).
- [12] F. Armero, and D. Ehrlich, Numerical modeling of softening plastic hinges in thin Euler-Bernoulli beams, *Comput. Struct.*, vol. 84, no. 10–11, pp. 641–656, 2006b. DOI: [10.1016/j.compstruc.2005.11.010](https://doi.org/10.1016/j.compstruc.2005.11.010).
- [13] J. Dujc, B. Brank, and A. Ibrahimbegovic, Multi-scale computational model for failure analysis of metal frames that includes softening and local buckling, *Comput. Methods Appl. Mech. Engrg.*, vol. 199, no. 21–22, pp. 1371–1385, 2010a. DOI: [10.1016/j.cma.2009.09.003](https://doi.org/10.1016/j.cma.2009.09.003).
- [14] A. Ibrahimbegovic, and D. Brancherie, Combined hardening and softening constitutive model of plasticity: precursor to shear slip line failure, *Comput. Mech.*, vol. 31, no. 1–2, pp. 88–100, 2003. DOI: [10.1007/s00466-002-0396-x](https://doi.org/10.1007/s00466-002-0396-x).
- [15] P. Jäger, P. Steinmann, and E. Kuhl, Modeling three-dimensional crack propagation – A comparison of crack path tracking strategies, *Int. J. Numer. Meth. Engng.*, vol. 76, no. 9, pp. 1328–1352, 2008. DOI: [10.1002/nme.2353](https://doi.org/10.1002/nme.2353).
- [16] M. Jukić, B. Brank, and A. Ibrahimbegović, Embedded discontinuity finite element formulation for failure analysis of planar reinforced concrete beams and frames, *Eng. Struct.*, vol. 50, pp. 115–125, 2013. DOI: [10.1016/j.engstruct.2012.07.028](https://doi.org/10.1016/j.engstruct.2012.07.028).
- [17] M. Jukić, B. Brank, and A. Ibrahimbegović, Failure analysis of reinforced concrete frames by beam finite element that combines damage, plasticity and embedded discontinuity, *Eng. Struct.*, vol. 75, pp. 507–527, 2014. DOI: [10.1016/j.engstruct.2014.06.017](https://doi.org/10.1016/j.engstruct.2014.06.017).
- [18] C. Linder, and F. Armero, Finite elements with embedded strong discontinuities for the modeling of failure in solids, *Int. J. Numer. Meth. Engng.*, vol. 72, no. 12, pp. 1391–1433, 2007. DOI: [10.1002/nme.2042](https://doi.org/10.1002/nme.2042).
- [19] O. L. Manzoli, and P. B. Shing, A general technique to embed non-uniform discontinuities into standard solid finite elements, *Comput. Struct.*, vol. 84, no. 10–11, pp. 742–757, 2006. DOI: [10.1016/j.compstruc.2005.10.009](https://doi.org/10.1016/j.compstruc.2005.10.009).
- [20] T. Saksala, D. Brancherie, and A. Ibrahimbegovic, Numerical modelling of dynamic rock fracture with a combined 3d continuum visco-damage embedded discontinuity model, *Int. J.*

- Numer. Anal. Meth. Geomech., vol. 40, no. 9, pp. 1339–1357, 2016. DOI: [10.1002/nag.2492](https://doi.org/10.1002/nag.2492).
- [21] A. Stanić, B. Brank, and D. Brancherie, Fracture of quasi-brittle solids by continuum and discrete-crack damage models and embedded discontinuity formulation, Eng. Fract. Mech., vol. 227, pp. 106924, 2020. DOI: [10.1016/j.engfracmech.2020.106924](https://doi.org/10.1016/j.engfracmech.2020.106924).
- [22] M. Ambati, R. Kruse, and L. D. Lorenzis, A phase-field model for ductile fracture at finite strains and its experimental verification, Comput. Mech., vol. 57, no. 1, pp. 149–167, 2016. DOI: [10.1007/s00466-015-1225-3](https://doi.org/10.1007/s00466-015-1225-3).
- [23] P. Areias, T. Rabczuk, and M. A. Msekh, Phase field analysis of finite-strain plates and shells including element subdivision, Comput. Methods Appl. Mech. Engrg., vol. 312, pp. 322–350, 2016. DOI: [10.1016/j.cma.2016.01.020](https://doi.org/10.1016/j.cma.2016.01.020).
- [24] J. Kiendl, M. Ambati, L. D. Lorenzis, H. Gomez, and A. Reali, Phase field description of brittle fracture in plates and shells, Comput. Methods Appl. Mech. Eng., vol. 312, pp. 374–394, 2016. DOI: [10.1016/j.cma.2016.09.011](https://doi.org/10.1016/j.cma.2016.09.011).
- [25] G. Lancioni, and G. Royer-Carfagni, The variational approach to fracture mechanics. A practical application to the French Pantheon in Paris, J. Elasticity, vol. 95, no. 1–2, pp. 1–30, 2009. DOI: [10.1007/s10659-009-9189-1](https://doi.org/10.1007/s10659-009-9189-1).
- [26] J. Reinoso, M. Paggi, and C. Linder, Phase field modeling of brittle fracture for enhanced assumed strain shells at large deformations: formulation and finite element implementation, Comput. Mech., vol. 59, no. 6, pp. 981–1001, 2017. DOI: [10.1007/s00466-017-1386-3](https://doi.org/10.1007/s00466-017-1386-3).
- [27] T. Pian, and K. Sumihara, Rational approach for assumed stress finite elements, Int. J. Numer. Meth. Engrg., vol. 20, no. 9, pp. 1685–1695, 1984. DOI: [10.1002/nme.1620200911](https://doi.org/10.1002/nme.1620200911).
- [28] M. Bischoff, E. Ramm, and D. Braess, A class of equivalent enhanced assumed strain and hybrid stress finite elements, Comput. Mech., vol. 22, no. 6, pp. 443–449, 1999. DOI: [10.1007/s004660050378](https://doi.org/10.1007/s004660050378).
- [29] C. McAuliffe, and H. Waisman, A Pian-Sumihara type element for modeling shear bands at finite deformation, Comput. Mech., vol. 53, no. 5, pp. 925–940, 2014. DOI: [10.1007/s00466-013-0940-x](https://doi.org/10.1007/s00466-013-0940-x).
- [30] G. Yu, X. Xie, and C. Carstensen, Uniform convergence and a posteriori error estimation for assumed stress hybrid finite element methods, Comput. Methods Appl. Mech. Engrg., vol. 200, no. 29–32, pp. 2421–2433, 2011. DOI: [10.1016/j.cma.2011.03.018](https://doi.org/10.1016/j.cma.2011.03.018).
- [31] J. Dujc, B. Brank, and A. Ibrahimbegovic, Stress-hybrid quadrilateral finite element with embedded strong discontinuity for failure analysis of plane stress solids, Int. J. Numer. Meth. Engrg., vol. 94, no. 12, pp. 1075–1098, 2013. DOI: [10.1002/nme.4475](https://doi.org/10.1002/nme.4475).
- [32] J. Schröder, M. Igelbüscher, A. Schwarz, and G. Starke, A Prange-Hellinger-Reissner type finite element formulation for small strain elasto-plasticity, Comput. Methods Appl. Mech. Engrg., vol. 317, pp. 400–418, 2017. DOI: [10.1016/j.cma.2016.12.005](https://doi.org/10.1016/j.cma.2016.12.005).
- [33] J. Dujc, B. Brank, and A. Ibrahimbegovic, Quadrilateral finite element with embedded strong discontinuity for failure analysis of solids, Comput. Model. Eng. Sci., vol. 69, no. 3, pp. 223–260, 2010b.
- [34] A. Ibrahimbegovic, 2009. Nonlinear Solid Mechanics: Theoretical Formulations and Finite Element Solution Methods, Springer, Dordrecht.
- [35] D. Y. Gao, Pure complementary energy principle and triality theory in finite elasticity, Mech. Res. Commun., vol. 26, pp. 31–37, 1999.
- [36] J. Dujc, B. Brank, A. Ibrahimbegovic, and D. Brancherie, An embedded crack model for failure analysis of concrete solids, Computers Concrete., vol. 7, no. 4, pp. 331–346, 2010c. DOI: [10.12989/cac.2010.7.4.331](https://doi.org/10.12989/cac.2010.7.4.331).
- [37] M. Lavrenčić, and B. Brank, Hybrid-mixed shell quadrilateral that allows for large solution steps and is low-sensitive to mesh distortion, Comput. Mech., vol. 65, no. 1, pp. 177–192, 2020. DOI: [10.1007/s00466-019-01759-3](https://doi.org/10.1007/s00466-019-01759-3).
- [38] J. Y. Wu, F. B. Li, and S. L. Xu, Extended embedded finite elements with continuous displacement jumps for the modeling of localized failure in solids, Computer Methods Appl. Mech. Eng., vol. 285, pp. 346–378, 2015. DOI: [10.1016/j.cma.2014.11.013](https://doi.org/10.1016/j.cma.2014.11.013).
- [39] M. Cervera, M. Chiumenti, and D. D. Capua, Benchmarking on bifurcation and localization in J_2 plasticity for plane stress and plane strain conditions, Comput. Methods Appl. Mech. Engrg., vol. 241–244, pp. 206–224, 2012. DOI: [10.1016/j.cma.2012.06.002](https://doi.org/10.1016/j.cma.2012.06.002).
- [40] J. Korelc, and P. Wriggers, 2016. Automation of Finite Element Methods, Springer International Publishing, Switzerland.
- [41] J. Korelc, 2020. AceGen, AceFem. <http://www.fgg.uni-lj.si/Symech>.
- [42] P. Fuschi, D. Perić, and D. R. J. Owen, Studies on generalized midpoint integration in rate-independent plasticity with reference to plane-stress j_2 -flow theory, Comput. Struct., vol. 43, no. 6, pp. 1117–1133, 1992. DOI: [10.1016/0045-7949\(92\)90012-O](https://doi.org/10.1016/0045-7949(92)90012-O).
- [43] J. Dujc, and B. Brank, Stress resultant plasticity for shells revisited, Comput. Methods Appl. Mech. Eng., vol. 247–248, pp. 146–165, 2012. DOI: [10.1016/j.cma.2012.07.012](https://doi.org/10.1016/j.cma.2012.07.012).
- [44] J. Mosler, A novel algorithmic framework for the numerical implementation of locally embedded strong discontinuities, Comput. Methods Appl. Mech. Engrg., vol. 194, no. 45–47, pp. 4731–4757, 2005. DOI: [10.1016/j.cma.2004.11.015](https://doi.org/10.1016/j.cma.2004.11.015).

Appendix A. Division of $\hat{\mathbf{G}}_m$

By using (33) in (10)-(13), we obtain the following regular and singular parts of $\hat{\mathbf{G}}_m$:

$$\hat{\mathbf{G}}_1 = \bar{\bar{\mathbf{G}}}_1 + \underbrace{\delta_\Gamma(\mathbf{x})\mathbf{B}_n\mathbf{n}}_{\bar{\bar{\mathbf{G}}}_1}, \quad (99)$$

$$\hat{\mathbf{G}}_2 = \bar{\bar{\mathbf{G}}}_2 + \underbrace{\delta_\Gamma(\mathbf{x})\mathbf{B}_n\mathbf{n}\zeta_\Gamma(\mathbf{x})}_{\bar{\bar{\mathbf{G}}}_2}, \quad (100)$$

$$\hat{\mathbf{G}}_3 = \bar{\bar{\mathbf{G}}}_3 + \underbrace{\delta_\Gamma(\mathbf{x})\mathbf{B}_n\mathbf{m}}_{\bar{\bar{\mathbf{G}}}_3}, \quad (101)$$

$$\hat{\mathbf{G}}_4 = \bar{\bar{\mathbf{G}}}_4 + \underbrace{\delta_\Gamma(\mathbf{x})\mathbf{B}_n\mathbf{m}\zeta_\Gamma(\mathbf{x})}_{\bar{\bar{\mathbf{G}}}_4}, \quad (102)$$

where

$$\bar{\bar{\mathbf{G}}}_1 = \bar{\mathbf{G}}_1 - \frac{1}{A_{\Omega^e}} \int_{\Omega^e} \bar{\mathbf{G}}_1 d\Omega - \frac{l_\Gamma}{A_{\Omega^e}} \mathbf{B}_n\mathbf{n}, \quad (103)$$

$$\bar{\bar{\mathbf{G}}}_2 = \bar{\mathbf{G}}_2 - \frac{1}{A_{\Omega^e}} \int_{\Omega^e} \bar{\mathbf{G}}_2 d\Omega, \quad (104)$$

$$\bar{\bar{\mathbf{G}}}_3 = \bar{\mathbf{G}}_3 - \frac{1}{A_{\Omega^e}} \int_{\Omega^e} \bar{\mathbf{G}}_3 d\Omega - \frac{l_\Gamma}{A_{\Omega^e}} \mathbf{B}_n\mathbf{m}, \quad (105)$$

$$\bar{\bar{\mathbf{G}}}_4 = \bar{\mathbf{G}}_4 - \frac{1}{A_{\Omega^e}} \int_{\Omega^e} \bar{\mathbf{G}}_4 d\Omega. \quad (106)$$

Appendix B. Definition of $\mathbf{f}_{m,\alpha}^{\Omega^e}$, $\mathbf{f}_{m,\alpha}^{\Gamma^e}$ and tractions

By using (99)-(102) in (41) and considering $\int_{\Omega^e} \delta_\Gamma(\circ) d\Omega = \int_{\Gamma^e}(\circ) d\Gamma$, we obtain the following scalar equations for $\mathbf{f}_{m,\alpha}^e$ in (41):

$$\mathbf{f}_{1,\alpha}^e = t^e \underbrace{\int_{\Omega^e} \bar{\bar{\mathbf{G}}}_1^T \mathbf{S} \boldsymbol{\beta} d\Omega}_{\mathbf{f}_{1,\alpha}^{\Omega^e}} + t^e \underbrace{\int_{\Gamma^e} \mathbf{n}^T \mathbf{B}_n^T \mathbf{S} \boldsymbol{\beta} d\Gamma}_{\mathbf{f}_{1,\alpha}^{\Gamma^e}} = 0, \quad (107)$$

$$\mathbf{f}_{2,\alpha}^e = t^e \underbrace{\int_{\Omega^e} \bar{\bar{\mathbf{G}}}_2^T \mathbf{S} \boldsymbol{\beta} d\Omega}_{\mathbf{f}_{2,\alpha}^{\Omega^e}} + t^{(e)} \underbrace{\int_{\Gamma^e} \zeta_\Gamma \mathbf{n}^T \mathbf{B}_n^T \mathbf{S} \boldsymbol{\beta} d\Gamma}_{\mathbf{f}_{2,\alpha}^{\Gamma^e}} = 0, \quad (108)$$

$$f_{3,z}^e = t^e \int_{\Omega^e} \underbrace{\overline{\mathbf{G}}_3^T \mathbf{S} \boldsymbol{\beta} d\Omega}_{f_{3,z}^{\Omega^e}} + t^{(e)} \int_{\Gamma^e} \underbrace{\mathbf{m}^T \mathbf{B}_n^T \mathbf{S} \boldsymbol{\beta}}_{:=t_m} d\Gamma = 0, \quad (109)$$

$$f_{4,z}^e = t^e \int_{\Omega^e} \underbrace{\overline{\mathbf{G}}_4^T \mathbf{S} \boldsymbol{\beta} d\Omega}_{f_{4,z}^{\Omega^e}} + t^{(e)} \int_{\Gamma^e} \underbrace{\mathbf{m}^T \mathbf{B}_n^T \mathbf{S} \boldsymbol{\beta}}_{:=t_m} d\Gamma = 0. \quad (110)$$

The traction t_n equals the stress $\mathbf{n}^T \mathbf{B}_n^T \boldsymbol{\sigma}|_{\Gamma^e}$, and the traction t_m equals the stress $\mathbf{m}^T \mathbf{B}_n^T \boldsymbol{\sigma}|_{\Gamma^e}$, with t_n and t_m representing the normal and the tangential component of $\mathbf{t} = [t_n, t_m]^T$.

Appendix C. Components of the tangent stiffness matrix

By using (37), (39), and (58), we have

$$\mathbf{K}_{dd}^e = \mathbf{0}, \quad \mathbf{K}_{d\beta}^e = t^e \int_{\Omega^e} \mathbf{B}^T \mathbf{S} d\Omega, \quad \mathbf{K}_{d\alpha}^e = \mathbf{0}, \quad (111)$$

where $\mathbf{B} = [\mathbf{B}_1, \mathbf{B}_2, \mathbf{B}_3, \mathbf{B}_4]$. By using (46), (30), 77 and (58), we obtain

$$\mathbf{K}_{\beta d}^e = t^e \int_{\Omega^e} \mathbf{S}^T \mathbf{B} d\Omega, \quad (112)$$

$$\mathbf{K}_{\beta\beta}^e = t^e \int_{\Omega^e} \mathbf{S}^T \left(2 \left(\frac{d\overline{\phi}}{d\overline{\gamma}} \right)^{-1} (\mathbf{A} \mathbf{S} \boldsymbol{\beta}) \otimes \frac{d\overline{\phi}}{d\boldsymbol{\sigma}} - 2\overline{\gamma} \mathbf{A} - \mathbf{C}^{-1} \right) \mathbf{S} d\Omega,$$

$$\mathbf{K}_{\beta\alpha}^e = t^e \int_{\Omega^e} \mathbf{S}^T \overline{\mathbf{G}} d\Omega,$$

where $\overline{\mathbf{G}} = [\overline{\mathbf{G}}_1, \overline{\mathbf{G}}_2, \overline{\mathbf{G}}_3, \overline{\mathbf{G}}_4]$. By using (41)-(45) and (58), we finally have

$$\mathbf{K}_{zd}^e = \mathbf{0}, \quad \mathbf{K}_{z\beta}^e = t^e \int_{\Omega^e} \overline{\mathbf{G}}^T \mathbf{S} d\Omega, \quad (113)$$

$$\mathbf{K}_{z\alpha}^e = t^e \int_{\Gamma^e} \begin{bmatrix} k_{nm} & \xi_{\Gamma} k_{nm} & k_{nm} & \xi_{\Gamma} k_{nm} \\ \xi_{\Gamma} k_{nm} & \xi_{\Gamma}^2 k_{nm} & \xi_{\Gamma} k_{nm} & \xi_{\Gamma}^2 k_{nm} \\ k_{mm} & \xi_{\Gamma} k_{mm} & k_{mm} & \xi_{\Gamma} k_{mm} \\ \xi_{\Gamma} k_{mm} & \xi_{\Gamma}^2 k_{mm} & \xi_{\Gamma} k_{mm} & \xi_{\Gamma}^2 k_{mm} \end{bmatrix} d\Gamma,$$

where $\overline{\mathbf{G}} = [\overline{\mathbf{G}}_1, \overline{\mathbf{G}}_2, \overline{\mathbf{G}}_3, \overline{\mathbf{G}}_4]$, and $k_{nn} = \frac{\partial t_n}{\partial \overline{u}_n}$, $k_{nm} = \frac{\partial t_n}{\partial \overline{u}_m}$, $k_{mm} = \frac{\partial t_m}{\partial \overline{u}_n}$, $k_{mm} = \frac{\partial t_m}{\partial \overline{u}_m}$. The latter derivatives depend on a particular form of $\overline{\phi}$, see (93).